INFORMATION TO USERS

This material was produced from a microfilm copy of the original document. While the most advanced technological means to photograph and reproduce this document have been used, the quality is heavily dependent upon the quality of the original submitted.

The following explanation of techniques is provided to help you understand markings or patterns which may appear on this reproduction.

1. The sign or "target" for pages apparently lacking from the document photographed is "Missing Page(s)". If it was possible to obtain the missing page(s) or section, they are spliced into the film along with adjacent pages. This may have necessitated cutting thru an image and duplicating adjacent pages to insure you complete continuity.

2. When an image on the film is obliterated with a large round black mark, it is an indication that the photographer suspected that the copy may have moved during exposure and thus cause a blurred image. You will find a good image of the page in the adjacent frame.

3. When a map, drawing or chart, etc., was part of the material being photographed the photographer followed a definite method in "sectioning" the material. It is customary to begin photoing at the upper left hand corner of a large sheet and to continue photoing from left to right in equal sections with a small overlap. If necessary, sectioning is continued again — beginning below the first row and continuing on until complete.

4. The majority of users indicate that the textual content is of greatest value, however, a somewhat higher quality reproduction could be made from "photographs" if essential to the understanding of the dissertation. Silver prints of "photographs" may be ordered at additional charge by writing the Order Department, giving the catalog number, title, author and specific pages you wish reproduced.

5. PLEASE NOTE: Some pages may have indistinct print. Filmed as received.

74-23,376

CLEMENTS, Arthur Earhart, 1940-
CLOUD STRUCTURE IN THE SOUTH TROPICAL ZONE,
RED SPOT AND NORTH POLAR REGION OF JUPITER.

The University of Arizona, Ph.D., 1974
Astronomy

University Microfilms, A XEROX Company, Ann Arbor, Michigan

CLOUD STRUCTURE IN THE SOUTH TROPICAL ZONE,

RED SPOT AND NORTH POLAR REGION OF JUPITER

by

Arthur Earhart Clements

A Dissertation Submitted to the Faculty of the

DEPARTMENT OF ASTRONOMY

In Partial Fulfillment of the Requirements
For the Degree of

DOCTOR OF PHILOSOPHY

In the Graduate College

THE UNIVERSITY OF ARIZONA

1 9 7 4

THE UNIVERSITY OF ARIZONA

GRADUATE COLLEGE

I hereby recommend that this dissertation prepared under my

direction by _____ Arthur Earhart Clements _____

entitled _____ CLOUD STRUCTURE IN THE SOUTH TROPICAL ZONE, _____

_____ RED SPOT AND NORTH POLAR REGION OF JUPITER _____

be accepted as fulfilling the disse. :ation requirement of the

degree of _____ Doctor of Philosophy _____

_____   4/30/74
Dissertation Director   Date

After inspection of the final copy of the dissertation, the

following members of the Final Examination Committee concur in

its approval and recommend its acceptance:*

_____   29 April, 1974
_____   1 May 1974
_____   May 1 1974

_____   _____

_____   _____

*This approval and acceptance is contingent on the candidate's
adequate performance and defense of this dissertation at the
final oral examination. The inclusion of this sheet bound into
the library copy of the dissertation is evidence of satisfactory
performance at the final examination.

STATEMENT BY AUTHOR

This dissertation has been submitted in partial fulfillment of requirements for an advanced degree at The University of Arizona and is deposited in the University Library to be made available to borrowers under rules of the Library.

Brief quotations from this dissertation are allowable without special permission, provided that accurate acknowledgment of source is made. Requests for permission for extended quotation from or reproduction of this manuscript in whole or in part may be granted by the head of the major department or the Dean of the Graduate College when in his judgment the proposed use of the material is in the interests of scholarship. In all other instances, however, permission must be obtained from the author.

SIGNED: *Arthur Clements*

ACKNOWLEDGMENTS

TABLE OF CONTENTS

LIST OF TABLES

LIST OF TABLES--*Continued*

LIST OF ILLUSTRATIONS

ABSTRACT

Correct interpretation of many kinds of observational evidence
depends upon accurate knowledge of the structure, distribution, and
properties of the Jovian clouds. Previous spectroscopic studies have
established that at least two vertically distinct cloud layers exist in
the equatorial latitudes, but have yielded only approximate values for
the characteristics of these layers and no information about regional
differences in cloud structure. This research makes use of new observa-
tional and theoretical methods to derive parameters for three Jupiter
regions having different structures.

Regional observations were obtained by area scanning in two
wavelength passbands (each 100 Å wide), one centered at 8880 Å and lying
within a rather strong absorption band of methane, the other centered at
9215 Å and lying in a region free of significant molecular absorption.
On May 10, 1971, during a 5-hour period between the rise and set of the
Red Spot, Jupiter was repeatedly scanned along a line through the Spot's
center and parallel to the equator, and intensity profiles of the South
Tropical Zone containing the Spot at various stages of its transit of
the disk were accumulated. After the Spot had set, the North Polar Re-
gion was similarly scanned. Star observations were made to provide cal-
ibration and to monitor seeing.

Reduction of these observations yielded accurate limb-darkening
curves on an absolute intensity scale for each region and wavelength.
These were interpreted by finding theoretical, multiple-scattering

models (based on the "doubling" method) that would reproduce them. Traditional reflecting layer and semi-infinite scattering models cannot account for the observations; the two-layer cloud model is the simplest capable of doing so. A number of assumptions about the phase function of the cloud particles and the curve-of-growth behavior of the 8880 Å band were examined, and parameters for the resulting families of models that fit the observations are included and discussed in this work. If the 9215 Å observations are used to fix the single-scattering albedo of the cloud particles, the number of free parameters is reduced to the point where only a few models are allowed by the observations. Particular attention is given to these models in drawing conclusions about cloud structure.

Values found for the cloud and gas layer thicknesses depend upon which phase function and degree of band saturation are assumed, but the *relative* thicknesses of the layers in going from one region to another are remarkably independent of such assumptions. For instance, the upper cloud layer is consistently found to be about 1/5 as thick in the North Polar Region as it is in the South Tropical Zone (where the optical depth is about 1 for isotropic scattering). The thicknesses of the two methane layers (located above and between the cloud layers) are nearly the same in the Zone and North Polar Region, indicating that the cloud layers occur at about the same altitudes in the two regions. In both regions the upper methane layer is about 1/3 to 1/2 as thick as the lower.

The Red Spot, which is a conspicuous bright feature at 8880 Å but only barely distinguishable from its surroundings at 9215 Å, is found to be a structural anomaly confined largely to the *upper* cloud

layer. This layer is thicker (by as much as 50%) in the Spot than in

the Zone, and the cloudtops of the Spot extend to about 5 km greater al-

titude than those of the Zone.

INTRODUCTION

Hess (1951) was the first to suggest that the distribution of
brightness over the disk of a planet seen at the wavelength of an ab-
sorption band might yield information concerning atmospheric structure.
His proposal of photography using narrowband filters has been put into
practice as rapidly as advances in the technologies of interference fil-
ters, image tubes, and infrared film have permitted (Owen, 1969). Pub-
lished pictures of Jupiter (Owen, 1969; Owen and Mason, 1969; Kuiper,
1972) have been obtained in the strong methane band near 8900 Å. They
reveal much interesting detail, varying with latitude and time, but more
important, they indicate general and persistent patterns of behavior for
the various major cloud features seen previously at continuum wavelengths.

In the equatorial and temperate latitudes there is generally a
good correlation between the continuum belt-and-zone structure and the
pattern of dark and bright bands seen at 8900 Å. At 8900 Å the belts
are nearly always dark and the zones are nearly always light, just as in
the continuum, but the pattern of *relative* brightness can be different
from that seen in the continuum (Kuiper shows an excellent example of
this effect), implying that the belts and zones represent not only re-
gional differences in cloud albedo, but also differences in cloud struc-
ture that result in differing amounts of absorption. One case of
particular interest is noted by Kuiper (1972). In 1970 and 1971 he found
that both North and South Tropical Zones (near latitudes 22° N and S)
were relatively much brighter at 8900 Å than in the red continuum. On

1

the basis of this, he speculates that the cloudtops reach greater altitudes in these zones than in the other equatorial zones and suggests that these regions may be similar to the tropical convergence zones of the Earth in some respects.

The polar regions (actually latitudes higher than about 40°) show a different pattern of behavior. The lower polar latitudes appear darker in comparison with the equatorial regions, but considerably more so at 8900 Å than in the nearby continuum. In the highest latitudes bright polar caps (or polar "hoods") having indefinite lower-latitude boundaries are often seen at 8900 Å. Sometimes only one pole is hooded, but more usually both are although there seems to be a tendency for the South Pole to have the brighter hood (Owen and Mason, 1969). There are no analogs of these surprising features in the continuum photographs. Their origins are as yet unknown. Owen (1969) speculates that variable, high-level haze is responsible. This seems likely although it is puzzling that such haze is found *only* near the poles rather than more or less uniformly distributed over the disk (limb brightening at 8900 Å is not observed except at the poles). Perhaps the haze particles are not ammonia (as elsewhere), but methane. The solid could exist in equilibrium with the vapor if the upper-atmospheric temperature falls below about 90°K in the polar regions. Condensation of methane would not occur in more equatorial regions where the minimum temperature (that of the stratosphere) is known to be greater than 100°K (115°K seems the most likely value to Hunten, 1971).

The Great Red Spot has appeared as a prominent bright feature in 8900 Å photographs of Jupiter since the first was obtained during the

apparition of 1968; indeed, it is usually the brightest feature on the planet (Kuiper, 1972). Viewed at red and near infrared wavelengths in the continuum, however, the Red Spot is hard to distinguish from the South Tropical Zone, which nearly surrounds it, because the cloud albedos are so nearly the same. Clearly, the enhanced brightness of the Spot at 8900 Å must arise almost entirely from structural differences between it and the Zone. Two extreme possibilities can be supposed. The first is that the clouds of the two regions are quite similar in structure and properties except that the cloudtops reach to greater heights in the Spot; hence there is a thinner layer of absorbing methane above the Spot to reduce its reflectivity at 8900 Å. A second possibility is that the cloudtops everywhere occur at the same altitude but for one reason or another (a greater number density of scattering particles or a cloud layer of greater total optical thickness) sunlight is diffusely reflected at a smaller depth in the clouds of the Spot. The first explanation is adhered to by Kuiper (1972), who makes no mention of the second. Owen and Mason (1969) recognize that a combination of the two possibilities is probably the best explanation, but they are unable to conclude which has the greater weight. They have obtained a rough value for the altitude difference in the cloudtops required by the first possibility. From a spectrogram of the Spot including the equatorial regions, they estimate that the level of reflection for 8900 Å is about 6 km higher in the Spot than in the Equatorial Zone.

From what we have said about the qualitative features of the 8900 Å photographs, it is clear that Jovian cloud structure must be considerably more complicated than was supposed before 1969. From

continuum observations it was known that cloud albedo varies from feature to feature and changes with time and wavelength, but even here the underlying causes are almost entirely unknown. Now the 8900 Å observations have added new variables to be considered along with cloud albedo. First, there is the possibility that we are dealing not with a single cloud layer, but with a "sandwich" containing two or more cloud and haze layers. Second, there is the possibility that some of these layers (like the haze of the polar hoods) are present in some regions but absent from others. Third, there is the virtual certainty that the layers have different vertical thicknesses, optical depths, particle sizes, and volume densities, not only from one layer to another but also for the same layer from one location to another. Since all of these factors interact in a complicated way to produce the observed 8900 Å brightness distribution, it is not surprising that so little definite and quantitative information regarding structure has been extracted from the methane-band photographs.

Because we are faced with such a complicated situation involving many free parameters to be evaluated simultaneously by radiative-transfer analysis of observational evidence, it is important that the observations be made so as to satisfy two general requirements. First, they should be planned with the objective of maximizing sensitivity to the effects of structure and differences in structures. Second, the observational method must minimize noise and be insensitive to systematic effects other than those arising from atmospheric structure; the greater the accuracy of the observations, the better can we distinguish between the numerous possible structures that might reasonably be proposed.

The photographic method has the advantages that it is relatively rapid and provides comprehensive, two-dimensional information. However, because of the faintness of Jupiter in a passband only 100 to 200 Å wide centered on a spectral region where more than 80% of the incident sunlight is absorbed, and because of the generally low quantum efficiencies (particularly where image tubes are not used), longer exposures and emulsions of higher speed are required. As a result, 8900 Å photographs show more blur arising from seeing and from guiding problems and more "grain noise" than do continuum photographs. There are also problems with limited range of exposure, nonlinearity of response, and nonuniformity of response characteristics that are usually encountered in photography. Hence the photographic method satisfies the first of our requirements but fails the second on account of noise and the many potential sources of systematic error.

The photographic method is probably most useful for reconnaissance. It can be used to locate regions likely to have structural features that merit closer examination with more accurate methods, and it can be used to make qualitative surveys of regional differences at frequent intervals, i.e., to monitor the large-scale weather phenomena of Jupiter. The work of Kuiper (1972) demonstrates the usefulness of making nearly simultaneous photographs at 8900 Å *and* at nearby continuum wavelengths. Without information concerning differences in cloud albedo from region to region it is often difficult to tell whether a feature is bright at 8900 Å because of smaller methane absorption or merely because its continuum albedo is higher than that of its surroundings.

Another approach to making observations at the wavelength of a molecular absorption band was also pioneered by Hess (1953). He reasoned that information concerning atmospheric structure is contained in measurements of the strength of absorption as a function of position across a planetary disk, and this led him to obtain spectra of a number of points in the Equatorial Zone of Jupiter (a region of presumably uniform structure), from which he determined the center-to-limb variations of the weak CH_4 6190 Å and NH_3 6441 Å bands. Almost no increase in strength toward the limbs was found, indicating that the simple reflecting layer model for line formation is not valid for these bands. Similar results (reviewed by McElroy, 1969) have since been obtained for most of the weak bands of methane and ammonia in the visible and near infrared. The stronger methane bands (including the 8873 Å band) seem to generally show more of an increase in strength toward the limbs than the weak bands do, but still far less than the increase required by the reflecting layer model.

As McElroy points out, the observational material collected so far is rather confusing and sometimes contradictory. Evidently the center-to-limb variations depend upon which belt or zone is observed and which band is considered. Time variations are also likely to enter in. Still, there are some curious results that are not so easily accounted for. For example, Teifel (1969) found no difference in CH_4 6190 Å absorption between the Red Spot and the South Tropical Zone in February of 1969, whereas Owen's 8900 Å photos taken in late 1968 and early 1969 continue to show the Spot as a bright feature! In one sense this confusion is encouraging; it indicates that center-to-limb variations are

sensitive to what must be rather minor changes and differences in struc-
ture and it shows that bands of differing strength can be used to probe
for details of structure at different depths within the clouds.

The usual method of approach in observational studies of
center-to-limb variations of band strength is well illustrated by the
recent work of Bergstralh (unpublished). He obtained coudé spectra of
the $3\nu_3$ band of methane at 11,000 Å using 14 different positions and
orientations of the spectrograph slit to obtain spatial resolution on
the disk of Jupiter. Even though an image tube was employed to increase
speed, each spectrum required guided exposures lasting from 3 hours
(near the center of the disk) to 6 hours (near the limbs). Spectra were
obtained between December 1969 and June 1970, requiring 16 nights' use
of the McDonald Observatory 82-in. telescope. Equivalent widths of four
rotational lines of the R branch of the band were measured by planimetry
of microphotometer tracings of spectra obtained with the slit in the
pole-to-pole orientation. Values representing averages over half the
pole diameter (including both belts and zones) were obtained because
this was "the minimum width that could be traced with signal/noise ade-
quate for quantitative analysis." The final result for each line was a
set of seven measures of the equivalent width corresponding to seven lo-
cations along the equator between one limb and the other. The reader is
referred to Bergstralh's paper for detailed discussion of the sources of
random and systematic errors; for our purposes it is sufficient to cite
his conclusion that, "as a conservative estimate, the accuracies of in-
dividual equivalent width measurements from the photographic spectra
should be better than 20 per cent."

Although the difficulties encountered in measuring individual lines of a strong band like the $3\nu_3$ are admittedly more severe than in most cases, this example makes clear the need for faster and more accurate methods of obtaining measurements of center-to-limb variations. Teifel (1969) has introduced some improvements. For example, he has substituted photoelectric spectrophotometry for photographic spectroscopy in some of his work, and he has investigated the use of measurements of the *depth* of bands like CH₄ 6190 Å in place of equivalent widths. Our observational method (described in detail in the next section of this paper) extends these approaches still further. We have used photoelectric *area* scanning to measure center-to-limb variations of *brightness* in fixed-wavelength passbands similar to those used in 8900 Å photography, one of which lies in the infrared continuum near the band wavelength. This method takes full advantage of the greater speed, accuracy, and spatial resolution possible with photoelectric photometry, yet it yields the same kind of information as gotten from the spectroscopically determined equivalent widths. Our observations of the limb darkening of the South Tropical Zone at 8880 Å *and* at 9215 Å were obtained in just 4 hours with accuracy better than a few per cent and spatial resolution on the order of an arc second. Our observations of the Red Spot and North Polar Region obtained on the same night show that it is possible to obtain results with poorer but still useful accuracy in even shorter periods of time.

Analysis and interpretation of the limb-darkening observations was done by matching the observational curves with theoretical curves derived from three types of structural models: (1) reflecting layer

models of the kind used in past years to determine molecular abundances
from spectroscopic observations, (2) semi-infinite scattering models
(e.g., McElroy, 1969), and (3) two-layer cloud models of the kind sug-
gested by the work of Danielson and Tomasko (1969), Lewis (1969), and
Owen (1969). The first two types are now considered too unrealistic,
but we considered it useful to demonstrate their complete inadequacy to
account for our observations. The two-cloud model has recently found
favor. It has been used successfully by Axel (1972) to interpret
whole-disk measures of equivalent widths for the H_2 quadrupole lines,
and by Bergstralh (unpublished) in the interpretation of the
center-to-limb measurements of equivalent width previously described.

Unfortunately, nearly all interpretations now in the literature
make use of rather approximate treatments of radiative transfer and as-
sume unrealistic isotropic scattering. Only the theoretical study of
line formation by Hunt (1973) includes consideration of the forward
scattering suitable for realistic clouds. Others have made use of the
method of van de Hulst-Grossman scaling to apply results derived from
isotropic scattering to more realistic clouds, even though (as we shall
see) this procedure is dubious in the case of the outer planets. Our
models have been computed assuming not only isotropic scattering but
also scattering like that of common types of terrestrial clouds. We
have used the powerful "doubling" method of radiative transfer intro-
duced by Hansen (1969a) to compute the reflection and transmission prop-
erties of the cloud layers, and we have used these in turn in computing
the reflectivity of multilayered inhomogeneous model atmospheres using
methods similar to the "adding" method described, for example, by Lacis

and Hansen (1974). Reflectivity obtained in this way is exact for all
practical purposes and includes all orders of scattering and all possi-
ble pathways of escape for incident photons. It is our hope that this
work demonstrates the advantages of these methods to the extent that
they come into general use, replacing the less rigorous approaches re-
ferred to above.

After describing the observational methods and results, the re-
mainder of this paper will be concerned with the theoretical models.
First we shall describe in some detail how reflectivity is computed for
the various structures considered. Next, we shall concern ourselves with
the fitting of the observational limb-darkening curves with theoretical
ones based on various assumptions with regard to scattering and absorp-
tion, examining the resulting models for similarities and differences
with the aim of deriving generalities useful not only in our work but
also in future investigations of atmospheric structure. Finally, we
shall narrow our attention to the most likely possibilities for the
three regions of Jupiter, comparing the structures found in order to de-
termine what variables are significant in producing the pattern of
brightness seen in the 8900 Å photographs.

OBSERVATIONS

Instrumentation and Observational Methods

Our observations of Jupiter were obtained with an area-scanning photopolarimeter used at the cassegrainian focus ($f/13$) of the 61-in. telescope of the Lunar and Planetary Laboratory, situated in the Santa Catalina Mountains near Tucson, Arizona. This instrument (which we used as a two-channel photometer rather than as a polarimeter) was derived from that described by Gehrels and Teska (1960) and by Coyne and Gehrels (1967) by the addition of an aperture holder that is moved back and forth along a line in the focal plane by a motor-driven screw whose precise position is measured as a voltage using a 10-turn potentiometer. The electronics were modified by replacing the current integrator with an amplifier and analog-to-digital converter that allowed sampling (and paper tape readout) of the signal at short intervals while the aperture scanned a line through the telescopic image. The two detectors were RCA 7102 photomultipliers with S-1 photocathodes suitable for the near infrared.

Jupiter was observed in two wavelength bands, each about 100 $\overset{\circ}{A}$ wide, which were isolated by the interference filters whose spectral transmission curves are shown in Fig. 1. One of these is centered at 8880 $\overset{\circ}{A}$ and lies within the limits of the CH_4 8873 absorption band; the other is centered at 9215 $\overset{\circ}{A}$ and lies within a rather narrow region that is apparently free of any important molecular absorption lines (judging from the high resolution spectra of Owen, 1969).

11
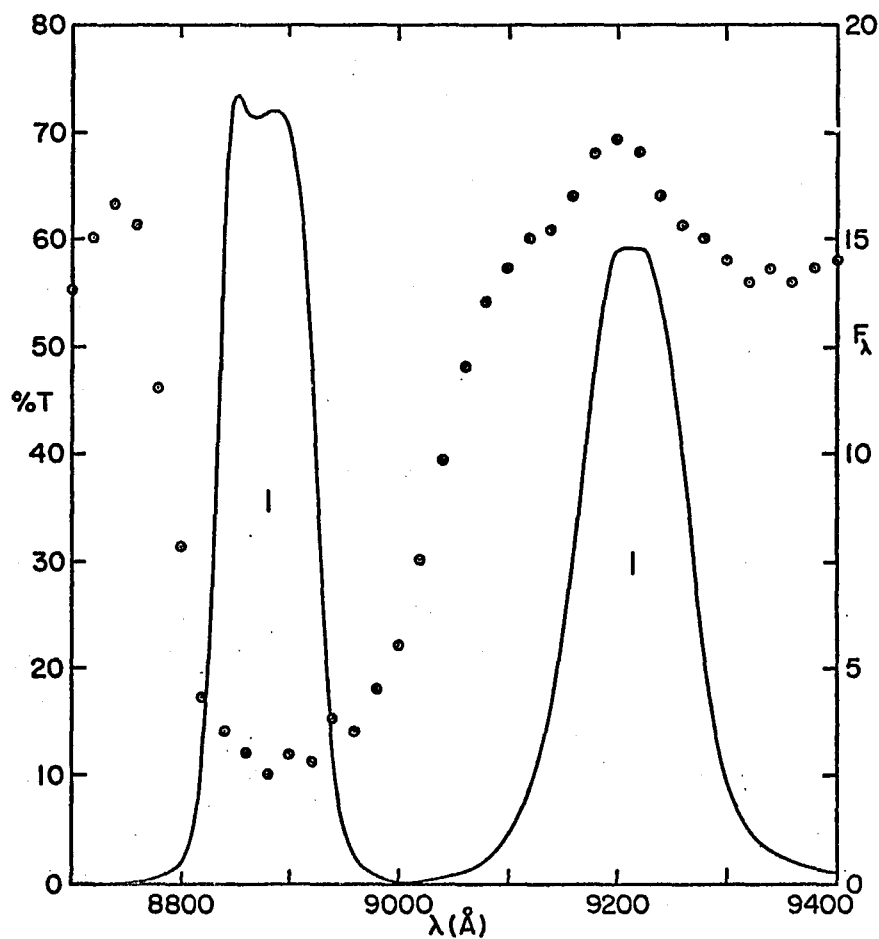
Fig. 1. Transmissions of Filters Compared with the Jovian
Spectrum.

The percentage transmissions of the 8880 and 9215 Å
interference filters (solid curves) are presented
on the same wavelength scale as the spectral flux
densities (circled dots) from the whole disk of
Jupiter measured by Taylor (1965). F_λ is in units
of 10^{-9} ergs sec^{-1} cm^{-2} Å^{-1}.

All of the scanner observations discussed in this work were ob-
tained within a 4-hour period during the night of 10 May 1971, at a time
when the equatorial diameter of Jupiter was 44.9 arc seconds and the
phase angle was only 2.7 degrees. The disk of the planet was scanned
along two lines parallel to its equator (see Fig. 2). Each back or
forth crossing required about 1 minute. A circular aperture with diame-
ter slightly greater than 1 arc second was used for Jupiter.

The schedule of observations (Table 1) shows that most of the
observation period was used to repeatedly scan through the center of the
Red Spot and along the South Tropical Zone, following the Spot's motion
across the disk from shortly after its first appearance, through its
transit of the central meridian at 7:51 U.T., and until it became indis-
tinguishable near the sunset edge of Jupiter's disk. The scans were
grouped in time and wavelength; each group was made up of four to eight
single-pass scans where the same wavelength was measured in duplicate by
the two channels. The time intervals between these groups were occupied
with changing filters, adjusting centering of the aperture on the Red
Spot latitude, photographing the planet, and the like. After the Spot
set, the shadow of the satellite Ganymede was used as latitude reference
for scans of the North Polar Region made parallel to the equator.

The intensity-versus-distance profiles resulting from one-time
scans are quite noisy because of the low signal strengths encountered in
using such narrow wavelength passbands, in using photocathodes with rel-
atively low quantum efficiencies, and (in the case of the 8880 $\overset{\circ}{A}$ scans)
in observing a wavelength region where the planet's surface brightness
is greatly reduced by methane absorption. Hence the first step in the

S

X ————————————————————— X′

−22°

45° 60°   0°

0°

10 arc sec

Y ————————————————————— Y′
+50°

o

N
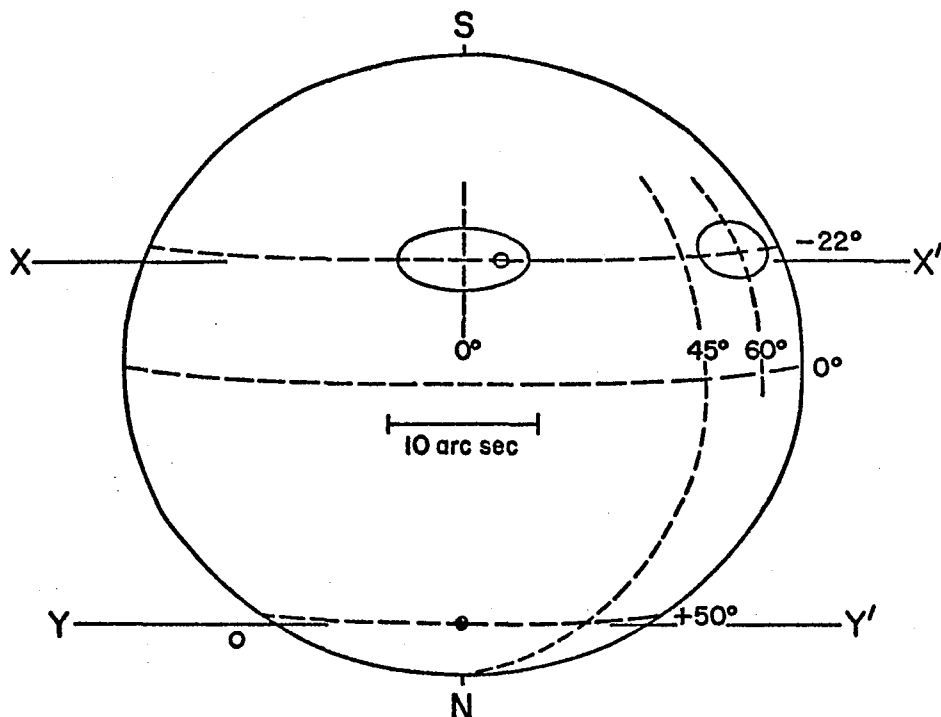
Fig. 2.   The Apparent Disk of Jupiter During the Observation Period.

The appearance of Jupiter's disk on 10 May 1971, showing the
Red Spot at central-meridian transit and in its foreshortened
aspect near the limb. Dashed lines indicate latitudes 22°S,
0°, and 50°N and also longitudes 0°, 45°, and 60° (measured
from the central meridian). The line XX′ is the scan line
across the Red Spot and South Tropical Zone; the small circle
within the Spot represents the size of the scanning aperture
used. The line YY′ is the scan line across the North Polar
Region; the positions of Ganymede and its shadow at the
time of scanning are indicated by open and filled circles,
respectively.

Table 1. Schedule of Observations of the Night of 10 May 1971.

Midtime (U.T.)	Object scanned	No. of scans	Wave-length	Remarks
5:53	Lambda Serpentis	6	8880 Å	Star obs. for calibration
5:57	"	6	9215	"
6:05	Jupiter photography		(Blue)	Kodak Panchromatic 140B film
6:18	Spot and Zone	6	8880	Red Spot just entirely risen
6:28	"	5	9215	
6:35	"	6	8880	
6:40	Jupiter photography			
6:46	Spot and Zone	5	8880	
6:54	"	6	9215	
7:01	"	6	8880	
7:08	"	6	9215	
7:19	"	6	8880	
7:25	Jupiter photography			
7:29	Spot and Zone	4	8880	
7:37	"	6	9215	
7:46	"	6	8880	
7:50	Jupiter photography			Red Spot close to central meridian
7:56	Spot and Zone	6	8880	
8:04	"	5	8880	
8:11	"	6	9215	
8:35	"	7	8880	
8:46	Ganymede	9	(V filter)	
8:58	Spot and Zone	8	8880	
9:09	"	6	9215	
9:16	"	6	8880	
9:20	Jupiter photography			
9:27	Spot and Zone	5	8880	
9:35	"	6	8880	Red Spot beginning to set
9:45	North Polar Region	5	8880	Shadow of Ganymede near central meridian
9:55	"	3	9215	
(10:30	Polarimetry of small white oval feature on Jupiter)			
11:24	Lambda Serpentis	8	8880	Star obs. for calibration
11:27	"	5	9215	"

process of reducing the observations to useful form is to average to-
gether the individual scans comprising each group, omitting those few
scans showing obvious abnormalities arising from guiding errors, scin-
tillation, passing clouds, etc. This averaging improves the signal-to-
noise ratio and permits calculation of the noise level as the standard
deviation characterizing the scatter of individual measures about the
mean. Figures 3, 4, and 5 are examples of the intensity profiles that
result. They include sky and dark currents; intensity is uncorrected
for the effects of varying extinction and detector sensitivity, and the
duplicate measures in the two channels have not yet been combined, but
they are useful for separating the Spot from the adjacent Zone and for
observing changes in the Spot's profile as rotation carried it from limb
to terminator.

Comparison of Figs. 3 and 4 clearly shows that, although the
Spot is hard to distinguish from the Zone at 9215 Å, it is a conspicuous
bright area at the wavelength of the methane band. Comparison of Figs.
3 and 5 shows the fading of the Spot near the terminator. The profile
of the Spot is also noticeably narrower near the terminator than it is
near the central meridian because of foreshortening.

Reduction of the South Tropical Zone Observations

The objective of reduction is to put the observations in a form
such that they can be directly and reliably compared with theoretical
predictions. This means that Spot and Zone observations must be sepa-
rated, duplicate measurements must be combined into single limb-darkening
curves for each wavelength, the intensity scale must be converted from

5/10/71   JUPITER RS   FILTER 89   D GAINS   TAPE 7

SCAN NOS.   1   2   3   4   5   6
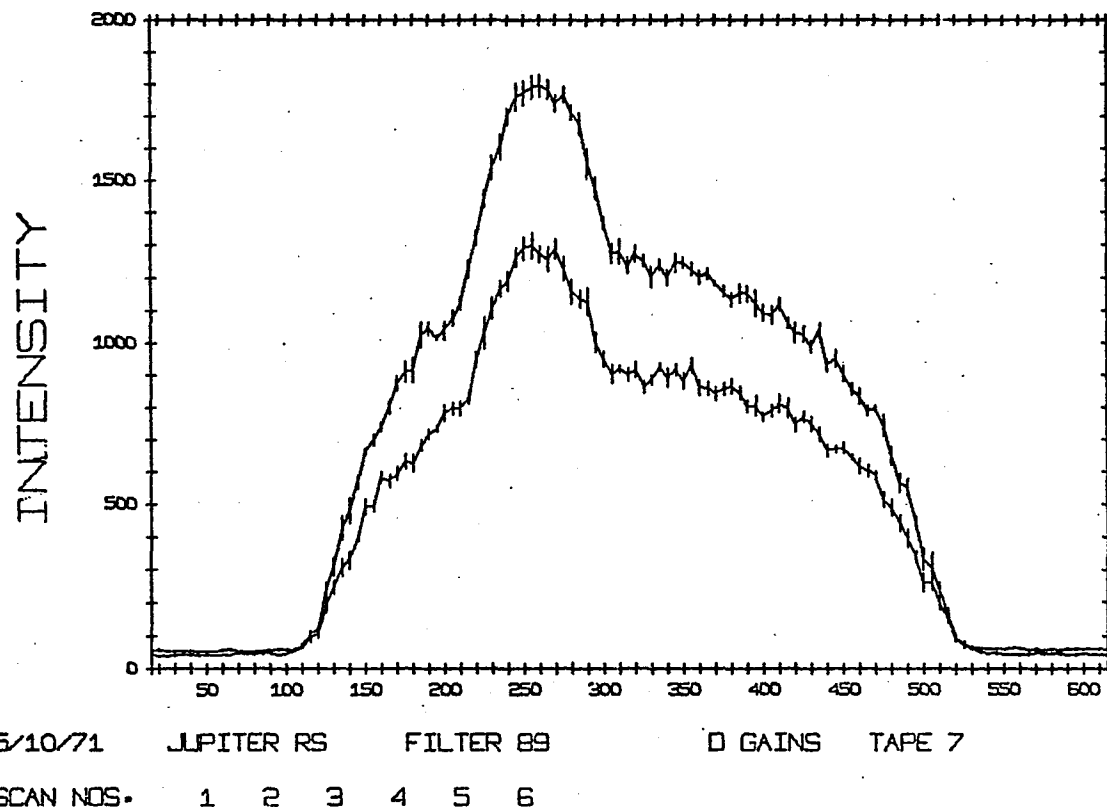
Fig. 3.   8880 Å Intensity Profiles across Jupiter at 7:19 U.T.

Relative intensity profiles (one for each of the two channels) across the
Red Spot and the South Tropical Zone for the wavelength of the methane
absorption band. The profiles were obtained by averaging six individual
scans (whose midtime was 7:19). Vertical lines along the profiles are
standard-deviation error bars. Distance scale is in potentiometer units
with an arbitrary zero point (one potentiometer unit is 0.1065 arc sec).
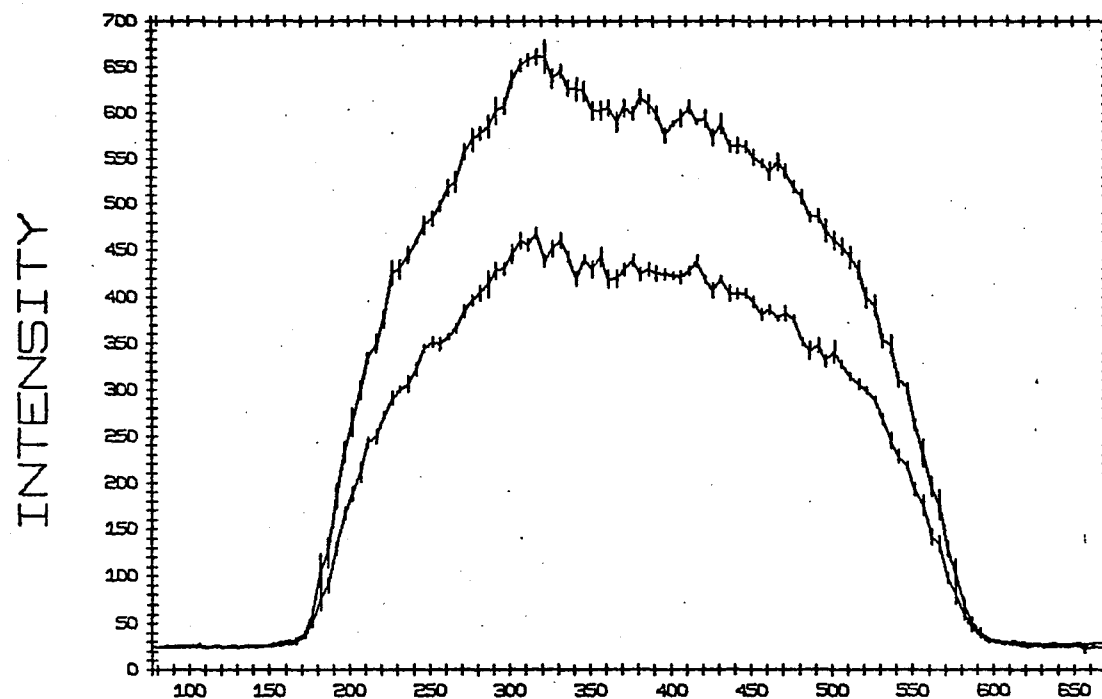
5/10/71   JUPITER RS   FILTER 92   C GAINS   TAPE 6

SCAN NOS. 104 105 106 107 108 109

Fig. 4.   9215 Å Intensity Profiles across Jupiter at 7:08 U.T.

Relative intensity profiles across the Red Spot and South
Tropical Zone for the infrared continuum wavelength.

Fig. 5.   8880 Å Intensity Profiles across Jupiter at 9:16 U.T.

instrumental counts to absolute units, and the instrumental scan coordi-
nates must be converted into the corresponding Jovian latitudes and lon-
gitudes. The remainder of this section describes the methods by which
these tasks were accomplished for the Zone observations, and following
sections describe methods used for the North Polar Region and Red Spot.

To start with, we have 14 Spot and Zone intensity profiles at
8880 Å and six at 9214 Å derived from the first stage of reduction. Be-
cause the Spot occupies only a small region of each profile, these are
mainly repeated measures of the limb darkening of the Zone which can be
combined into single curves having smaller noise levels. Furthermore,
because the observations extend over nearly half of a Jovian rotation
period, combining them largely averages out the effects of small longi-
tudinal variations of cloud albedo in the Zone.

The first step toward combination is the matching of the indi-
vidual profiles in the scan direction. It is important that this be
done accurately; otherwise, when the profiles are combined, the inten-
sity values averaged at each point along the curve will not all refer to
the same location on the planet, and a systematic broadening of the curve
results. We took one of the 8880 Å profiles and one of the 9215 Å pro-
files (both with the Spot near the center of the disk) as standards; the
x coordinate of the standard (in potentiometer units) becomes the stand-
ard X to which the x coordinate systems of all the other profiles are
related. The relation is found for each profile in turn by slide-fitting
it to the standard profile, moving the profile in the x direction until
the best over-all match of the two is found, then reading off the dif-
ference between profile x and standard X. The end result is that every

x value of every profile can be assigned a value of $X(8880)$ or $X(9215)$ that is uncertain by less than half an arc second at most.

Once the profiles are matched in the X direction, the matching along the intensity axis becomes possible. Because slowly changing extinction and instrumental sensitivity causes the intensity scales of the profiles to differ slightly, direct averaging of the X-matched profiles would lead to a spuriously high noise level (standard deviation) being computed. To avoid this, we again make use of our standard profiles, but now comparing each profile with the standard along the intensity axis. The differences between the two profiles (now both having sky and dark signals subtracted and regions affected by the Red Spot excised) are computed at all corresponding points, then summed after squaring. This is done repeatedly, each time multiplying all the intensities of the profile being matched by a scale factor near 1.0, until a factor is found that makes the sum of the squares of the differences a minimum.

When all of the profiles have been scaled in this way, they are averaged together to yield combined observational limb-darkening curves of the Zone. These are still relative curves (we have found it useful to normalize them to unity at the central meridian), but once the absolute intensity is known for one point, it is known for all. For observational reasons the absolute intensity is most reliably determined at points near the center of Jupiter's disk; hence we have chosen the intersection of the scan lines with the central meridian. Also, rather than measure intensity reflected at this point, we have found its reflectivity, G, because this is more directly compared with theoretical results.

This reflectivity is defined by

$$G = F_O/F_L = S/4\mu, \tag{1}$$

where F_O is the observed flux density from a small region on Jupiter, F_L is the flux density that would be observed if the Jupiter region were to be replaced by a unit-albedo Lambert surface perpendicular to the direction of the incident sunlight, S is Chandrasekhar's scattering function (which will be discussed in connection with theoretical models), and $\mu = \cos\theta$. (Frequently used mathematical symbols are listed in the Appendix.)

The Lambert flux densities (one for 8880 Å and one for 9215 Å) are found from

$$F_L = 2.350 \times 10^{-11} A F_S/\pi r^2, \tag{2}$$

where A is the area of the circular aperture used to scan Jupiter (found by photometric calibration to be 0.992 square arc seconds, corresponding to a diameter of 1.12 arc seconds), r is the distance of Jupiter from the sun in A.U., and F_S is the solar flux density at 1 A.U. distance (taken from the spectral irradiance tables of Labs and Neckel (1968), $F_S(8880) = 9.23 \times 10^{-2}$ and $F_S(9215) = 8.63 \times 10^{-2}$ W cm^{-2} μm^{-1}).

The observed flux densities of Jupiter are found by making use of star observations to calibrate instrumental sensitivity. For this purpose we chose the solar-type star Lambda Serpentis because (1) the absolute flux density, $F^*(\lambda)$, is known from the 13-color photometry of Mitchell and Johnson (1969), (2) the apparent brightness of this star is about the same as Jupiter seen through a small aperture and hence the measured signals (I^* and I, respectively) are similar and problems with

nonlinearity in the response of the photomultipliers are avoided, and
(3) this star and Jupiter could be observed at similar zenith distances,
thus minimizing errors arising from uncertainty in atmospheric extinc-
tion characteristics. Observed flux densities were found from

$$F_O = 10^{0.4k(x-x^*)} F^*(I_i/I_i^*), \tag{3}$$

where x and x^* are respectively the air masses of Jupiter and the star,
$k(\lambda)$ is the atmospheric extinction coefficient (in magnitudes per air
mass), I_i and I_i^* are signals measured in the ith channel, and F^* has
the same units as F_O and F_L.

We used mean extinction coefficients [k(8880) = 0.058 and k(9215)
= 0.055] taken from Mitchell and Johnson's values for many nights' pho-
tometry at the Catalina observatories. I_1 and I_2 values were taken from
combined Jupiter observations (x being that for the standard profile);
they are judged to be accurate to within a few per cent. Because of
somewhat higher noise levels in the star measures, uncertainties in I_1^*
and I_2^* are probably the most important source of uncertainty in the G
values derived. Even so, the internal agreement of values is always
better than 10%, leading us to adopt values (with approximate ranges) of
G(8880) = 0.12 ± 0.01 and G(9215) = 0.68 ± 0.05 for the South Tropical
Zone at the central meridian. The ratio G(8880)/G(9215) is in very good
agreement with the ratio of reduced fluxes F(8880)/F(9215) = 3/17 gotten
from the whole-disk spectrophotometry of Taylor (1965). Rough values of
G can be derived from Taylor's data by making the approximate assumption
that Jupiter's limb darkening follows Lambert's law; they are G(8880) $\simeq$
0.1 and G(9215) $\simeq$ 0.6.

Let us now consider the question of converting the standardized scan coordinate (X) into the corresponding Jovian latitude and longitude (l and L). Since the scan line through the Spot and along the Zone (see Fig. 2) quite closely follows a circle of latitude, we have made the approximation that the latitude is 22° South for all points on the limb-darkening curves of the Spot and Zone. For our purposes it is sufficient to define a relative longitude system with its origin fixed at the central meridian and with the positive L direction in the direction of planetary rotation. That is, $L = -90°$ for all points along the rising edge of the apparent disk, $L = 0°$ for all points along the central meridian, and $L = +90°$ for all points along the setting edge. Given this definition, X and L are related by

$$X = X_0 + X_l \sin L, \tag{4}$$

where X_0 is the value of X at the central-meridian point and X_l is half of the chordal width of the disk for a chord crossing parallel to the equator at latitude l. (Rigorously speaking, $X_l = R_l \cos l$, where R_l is the radius of the oblate planet at latitude l.)

The most direct method of applying Eq. (4) involves determining the constants X_0 and X_l by simply measuring them from the intensity profiles. The results, however, are not very accurate, mainly because the blur due to seeing makes it hard to definitely locate the positions corresponding to the edges of the disk. We have instead found these constants by a novel method that makes use of measurements of the location of a feature on the disk as a function of time. In our case, 14 values of $X(t)$ of the center of the Red Spot were measured, one from each of

the 8880 Å profiles, then 14 corresponding values of $L(t)$ were calcu-
lated by making use of the Red Spot's known rotation period and time of
central-meridian transit. These were then used in a least-squares solu-
tion for X_0 and X_l with Eq. (4) as the "equation of condition." The
constants determined in this way are so precise that Eq. (4) can be used
to convert $X(8880)$ into L with an uncertainty of less than $1°$ (when the
absolute value of L is less than about $70°$). Longitudes derived for the
9215 Å observations are somewhat less precise because Eq. (4) is used
with a different X_0, one found by slide-fitting of the 9215 and 8880 Å
combined limb-darkening curves, which is uncertain by a few tenths of an
arc second.

Our final consideration under the heading of reduction of the
Zone observations actually has more to do with the question of the re-
liability of the reduced values. Here we will be concerned with the
perturbations due to astronomical seeing. The ever-present turbulence
of the earth's atmosphere leads to blurring and spreading of the tele-
scopic image, which can introduce systematic errors into the observa-
tional limb-darkening curves. It is important to assess these errors
before undertaking theoretical analysis of the observations.

Seeing conditions during the observation period were good, and
the quality of the seeing remained almost constant. This qualitative
judgment by the observer is borne out by actual measures of the seeing
blur gotten by observing the star Lambda Serpentis at the beginning and
end of the Jupiter observation period. A rectangular aperture (6.0 by
30 arc seconds) large enough to contain the entire seeing-blurred image
of the star was repeatedly scanned across the center of it along a line

perpendicular to the aperture's longer axis. When the entire image lies within the aperture, the total brightness of the star (I^*) is measured for use in calibration as already described. When the star moves out of the aperture, an increasing fraction of its image is cut off by the aperture's edge. The measurements of signal strength versus aperture position that result contain detailed information about the radial distribution of brightness within the star image. That is, when these measurements are inverted by one means or another, they tell us precisely how seeing blurs the image of a point source, and hence we obtain the *blur function* or *point spread function* empirically.

For the degree of accuracy required in our case it is sufficient to assume that the blur function is approximated by a Gaussian form

$$I(r) = I_0 \exp[-(r/r_0)^2] \; ; \tag{5}$$

then the shape of the signal-versus-position curve is given by

$$S(x) = S_0 \int_{a(x)}^{b(x)} \exp(-u^2) \, du \, , \tag{6}$$

where $a = (x - \tfrac{1}{2}w)/r_0$, $b = (x + \tfrac{1}{2}w)/r_0$, w is the width of the (long) slit, and r_0 is the Gaussian parameter whose size characterizes the quality of the seeing. Fitting curves derived from Eq. (6) to our observations of Lambda Serpentis yields r_0 = 1.0 and 0.9 arc seconds for the start and end of the Jupiter observation period. These values are typical of very good seeing.

Comparison of r_0 with the apparent size of Jupiter's disk (about 40 arc seconds wide at latitude 22°S) makes it clear that no large-scale distortions of the limb-darkening curves by seeing are possible. Seeing

blur is short-range in its effects; when considering a given point in Jupiter's image we know that only points nearer than about 2 arc seconds can have any measurable perturbing effect. Furthermore, if the surface brightness is changing slowly over the distance scale of r_0, the *net* effects of seeing are negligible. In this case blur transfers about as much brightness to a given point from all surrounding points as it transfers from the point to the surroundings. Seeing can cause significant differences only between true and observed brightnesses in regions where true brightness changes rapidly on the distance scale of r_0, that is, near brightness discontinuities like the boundaries of the Red Spot and the limb or terminator of the planet.

Figure 6 illustrates these principles for the case of a chordal scan across Jupiter's limb. We have taken a hypothetical true brightness distribution to simulate that of Jupiter and blurred it with Gaussian seeing (r_0 = 1.065 arc second), using the convolution equation

$$I_{obs}(x,y) = \frac{1}{\pi r_0{}^2} \iint_{-\infty}^{\infty} I_{true}(x',y')\, e^{-(r/r_0)^2}\, dx'\, dy', \qquad (7)$$

where $r^2 = (x - x')^2 + (y - y')^2$. The results show that blurred and un-blurred intensity profiles virtually coincide at points interior to the disk, but when the limb is closer than 2 arc seconds the effects of seeing are important in proportion to the nearness to the limb. Applying these results to the case of our combined observational limb-darkening curves of the South Tropical Zone, we find that the points 2 arc seconds from limb or terminator lie at longitudes -63° and +63°, and hence points having longitudes outside these limits are suspect because of seeing; these points were omitted from further consideration.
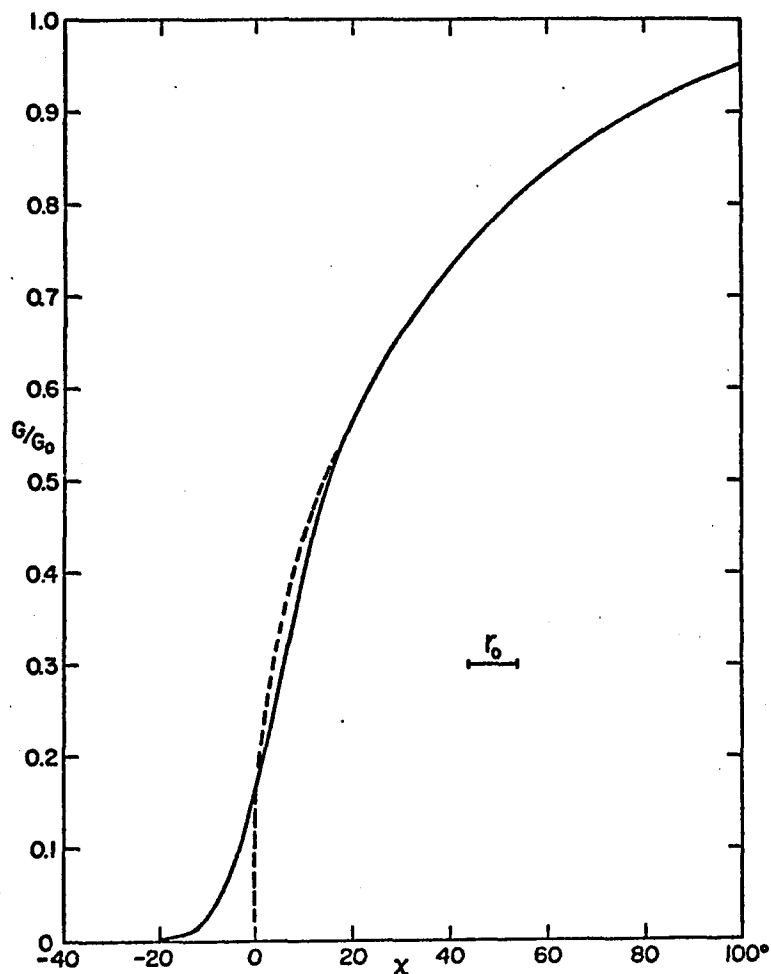
Fig. 6. Hypothetical Intensity Profiles Illustrating Seeing Effects.

The dashed curve is the relative intensity profile along a
scan line crossing the disk of Jupiter along latitude 22°S for
the case of no blur due to seeing. The solid curve represents
the case where the intensity distribution is affected by Gaus-
sian seeing blur having r_0 equal to 10 potentiometer units.
The x coordinate is in potentiometer units, and x is measured
along the scan line from the point of intersection of the scan
line with the limb. The intensity scale is relative to the
absolute brightness at the scan line's central-meridian point
(not shown).

The observational limb-darkening curves of the Zone in their final forms are shown in Figs. 7 and 8. Since there is little scatter in the points, smooth mean curves (not shown) can be drawn through them with confidence. Table 2 contains 13 values of G/G_0 for each wavelength taken from such curves. We have fitted theoretical limb-darkening curves (whose derivation is described beginning on page 39) as closely as possible to these few points (rather than to the 140 or so observation points), reasoning that the best fit to them is also very nearly the best possible fit to all of the observation points.

Table 2. Observational Mean Values Used in Fitting Models to the South Tropical Zone.

L	8880 $\overset{\circ}{A}$		9215 $\overset{\circ}{A}$	
	G/G_0	σ_0	G/G_0	σ_0
-60°	0.610	0.012	0.586	0.007
-54	0.695	0.015	0.667	0.007
-45	0.810	0.012	0.778	0.007
-30	0.938	0.015	0.913	0.010
-21	0.982	0.015	0.964	0.012
-9	1.001	0.010	1.000	0.015
0	1.000	0.008	1.000	0.008
9	0.984	0.010	0.989	0.007
21	0.945	0.011	0.935	0.007
30	0.897	0.009	0.867	0.010
45	0.740	0.013	0.713	0.006
54	0.607	0.012	0.605	0.004
60	0.508	0.010	0.524	0.006
$\overline{\sigma_0}$	--	0.012	--	0.008
G_0	0.12±0.01	--	0.68±0.05	--
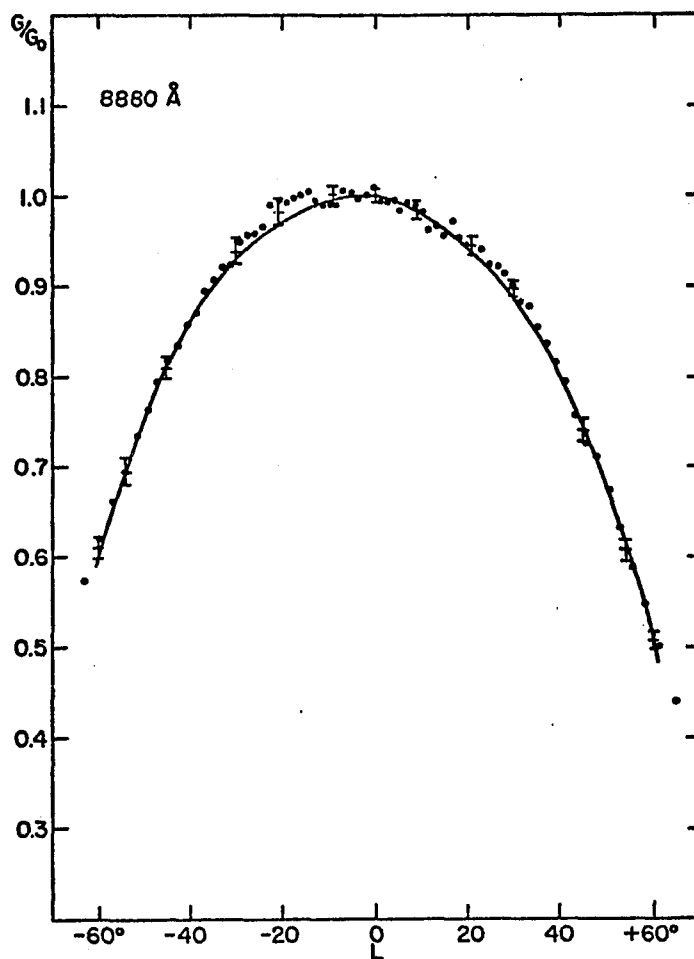
Fig. 7.   Combined 8880 Å Observations of the South Tropical Zone.

Combined methane-wavelength observations of limb darkening
in the South Tropical Zone (dots) compared with a theoret-
ical model (solid curve) fitted to the 13 points from the
mean curve through the data. The ⊥ symbols are standard
deviation error bars for the 13 observational-mean points.
The model is of the two-layer cloud type and assumes
cumulus/stratus scattering, saturated CH_4 absorption, and
$\omega_0 = 0.9958$. Model parameters derived from fitting are
$\tau_A = 0.550$, $\tau_L = 4.70$, and $\tau_B = 0.546$ (with fit sigma of
0.82×10^{-2}).
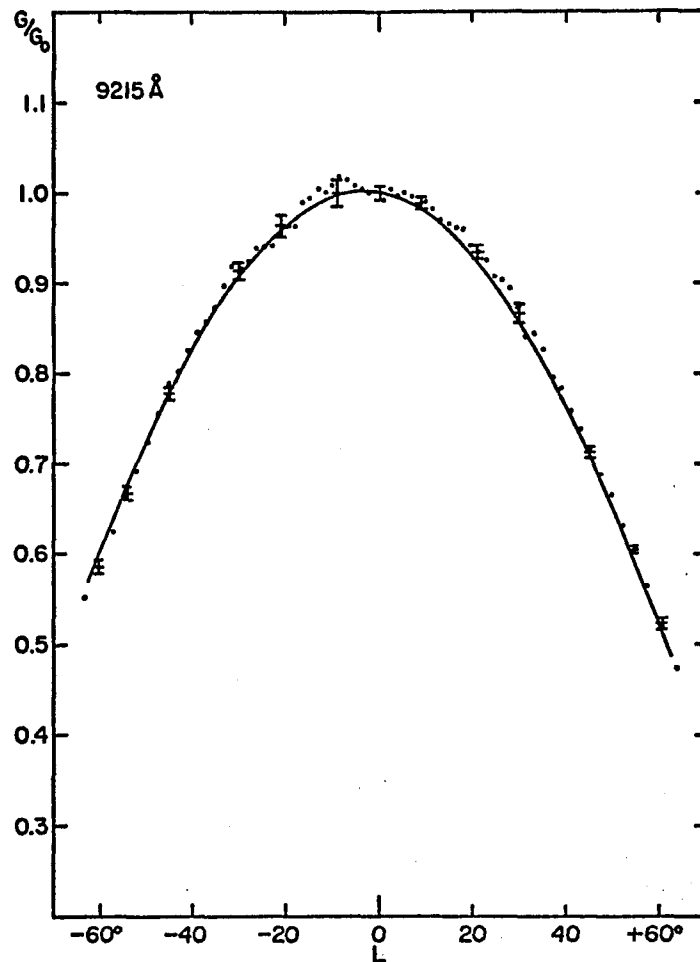
Fig. 8. Combined 9215 Å Observations of the South Tropical Zone.

Combined continuum-wavelength observations of limb darken-
ing in the South Tropical Zone compared with a theoretical
model curve. The model consists of a thin absorbing layer
overlying a semi-infinite, cumulus/stratus-scattering
cloud deck. The model parameters derived from fitting to
the 13 observational-mean points are $\omega_0 = 0.9958$ and $\tau_A = 0.0215$ (with fit sigma of 0.86×10^{-2}).

Reduction of the North Polar Region Observations

Scans of the North Polar Region (N.P.R.) were combined in much the same way as already described for the South Tropical Zone. Results are shown in Fig. 9. Because far fewer scans were made, and because the N.P.R. is less than half as bright as the Zone, the noise levels are higher. Also, since the period of observation was short, longitudinal albedo variations are not averaged out by combining; a small bright region is probably responsible for the peak seen in Fig. 9a near $L = +10°$.

The shadow of the satellite Ganymede transited the central meridian shortly before the N.P.R. scans were made, providing a means of accurately fixing the latitude observed. From the known spatial relationships of the satellite, the sun and Jupiter, we find that Ganymede's shadow intersected the planet's surface at latitude 50°N. In our pole-to-pole 8880 Å scans of 16 March 1971 this latitude is seen to lie near the center of a dark belt between the bright polar hood and the generally bright belt-and-zone structure of the equatorial regions. Our blue-light photographs show no recognizable belts or zones north of latitude 30°.

Because the curve of the limb intersects the chordal scan line more obliquely in the case of the N.P.R. than in the case of the South Tropical Zone, points 2 arc seconds from the limb and terminator occur at $L = ±45°$, rather than at $L = ±63°$, hence the smaller ranges of longitude in Fig. 9 and Table 3. Longitude assignments for the N.P.R. are uncertain by about 2 degrees because the constants X_0 and X_l had to be measured directly from the intensity profiles rather than being found by the least squares method.
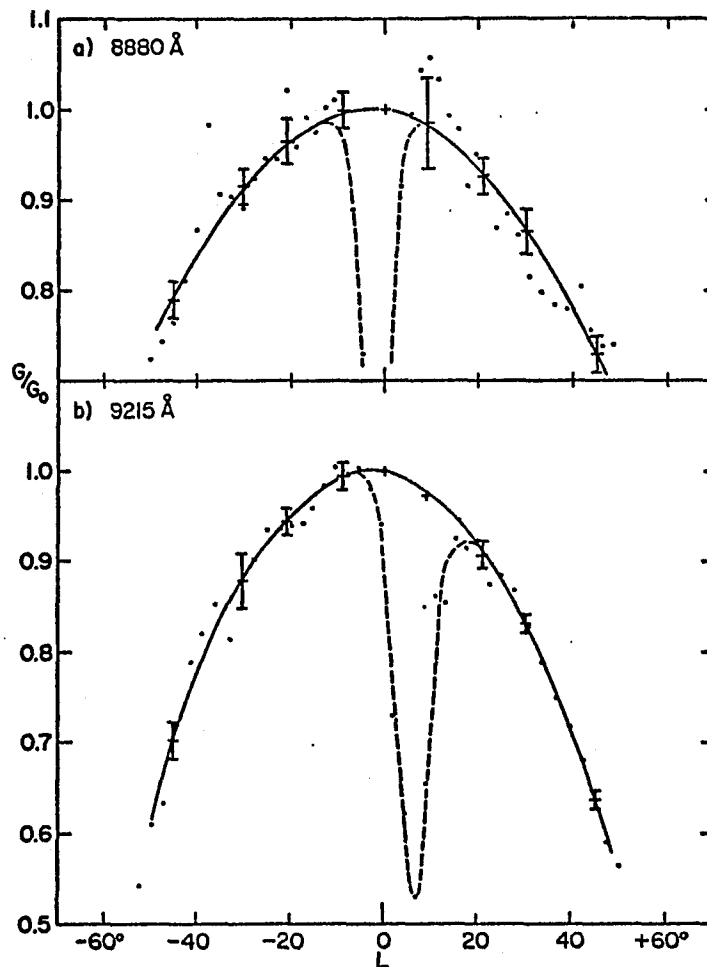
Fig. 9.   Combined 8880 Å and 9215 Å Observations of the North Polar
Region.

Combined limb-darkening observations for (a) the methane
wavelength and (b) the continuum wavelength. Dashed curves
show the shadow of Ganymede. Solid curves are for theoret-
ical models fitted to the observations. The model of (a)
is of the two-layer cloud type, assuming cumulus/stratus
scattering, saturated CH_4 absorption, and $\omega_0 = 0.9958$, and
fitting yields $\tau_A = 0.551$, $\tau_L = 0.75$, and $\tau_B = 0.737$ (with
fit sigma of 0.33×10^{-2}). The model of (b) consists of a
thin absorbing layer overlying a semi-infinite, cumulus/
stratus-scattering cloud deck, and fitting yields $\omega_0 = 0.9924$ and $\tau_A = 0.102$ (with fit sigma of 0.36×10^{-2}).

Table 3. Observational Mean Values Used in Fitting
          Models to the North Polar Region.

L	8880 Å		9215 Å	
	G/G_0	σ_0	G/G_0	σ_0
-45°	0.790	0.020	0.702	0.020
-30	0.916	0.020	0.879	0.030
-21	0.965	0.025	0.944	0.015
-9	0.999	0.020	0.944	0.015
0	(1.0)	--	(1.0)	--
9	0.986	0.050	(0.97)	--
21	0.927	0.020	0.908	0.015
30	0.865	0.025	0.832	0.010
45	0.730	0.020	0.638	0.010
$\overline{\sigma_0}$	--	0.025	--	0.016
G_0	0.04	--	0.33	--

Reduction of the Red Spot Observations

The case of the Red Spot differs from those of the Zone and
North Polar Region in that the limb-darkening curve of the Spot must be
built up, point by point, from single observations made at intervals
while the Spot is carried across the disk by Jupiter's rotation. The
reflectivity of the Spot as a function of longitude, $G(L)_S$, is most eas-
ily and accurately obtained from the intensity profiles by measuring the

ratio of the Spot's brightness to the brightness of the Zone at the same longitude:

$$R(L) = G(L)_S/G(L)_Z. \tag{8}$$

Because the reflectivity of the Zone is quite precisely known, the accuracy of the Spot's reflectivity depends mainly on the accuracy in measuring R. We have used two methods to obtain R, applying both to the I_1 and I_2 profiles separately.

The first method is simply to measure I_S and I_Z from the intensity profile. Obtaining I_Z requires interpolation of the Zone profile through the point directly under the center of the Red Spot peak, and there is sometimes considerable uncertainty involved in this. This method gives good reproducibility in measurements of R when applied to 8880 Å profiles where the Spot is not near the limb or terminator. Otherwise it is difficult to apply accurately, particularly in the case of the 9215 Å profiles, where the Spot is often barely distinguishable from the Zone. In such cases the second method yields the better R values. In this method the appropriate combined limb-darkening curve is scaled along the intensity axis so that it matches as closely as possible the Zone part of the profile being considered, and then the scaled curve is subtracted from the profile, leaving only a peak of height $I_S - I_Z$ at the position of the Red Spot. Because I_Z is already known from the scaled curve, $R = I_S/I_Z$ is immediately gotten. In cases where both methods could be applied, they yield similar R values. Final results for $R(L)$ are shown in Fig. 10 and Table 4. The standard deviation values (σ_R) given indicate the degree of internal agreement in R
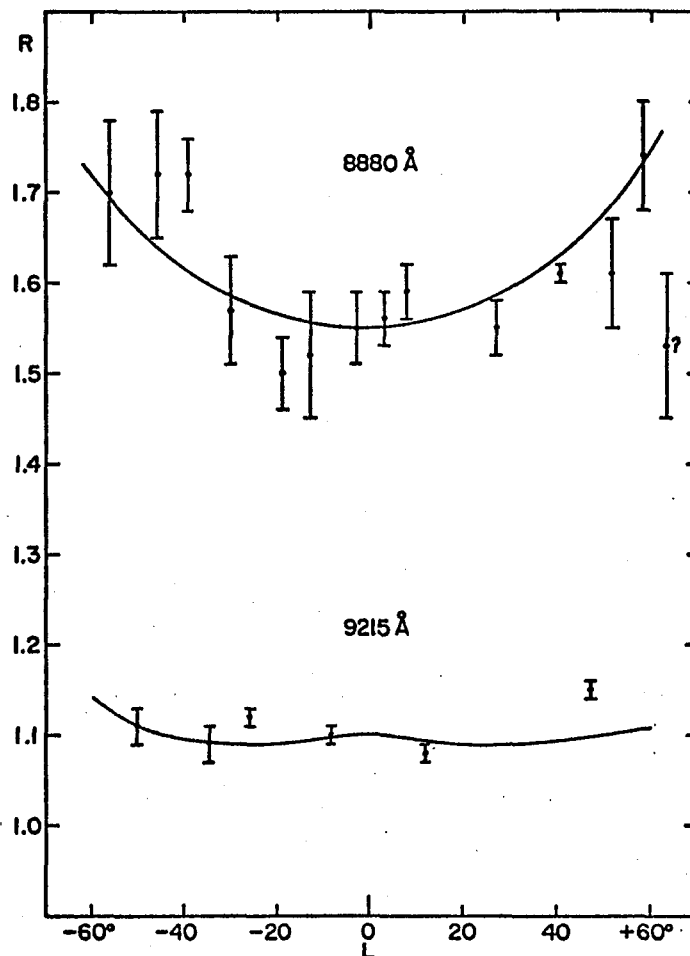
Fig. 10. Combined 8880 Å and 9215 Å Observations of the Red Spot.

Limb-darkening observations (with standard-deviation er-
ror bars) of the Red Spot at the methane wavelength (top)
and the continuum wavelength (bottom). The observations
are in the form of the ratio R of the Spot's brightness to
the Zone's brightness at the same longitude. The 8880 Å
observation at $L = 63°$ is of doubtful accuracy (see text).
The solid curves are for theoretical models. For 8880 Å,
the model assumes cumulus/stratus scattering, saturated
CH_4 absorption, $\omega_0 = 0.9958$, and $\tau_B = 0.547$, and fitting
yields $\tau_{AS} = 0.372$ and $\tau_{LS} = 5.70$ (with ratio fit sigma of
5.2×10^{-2}). For 9215 Å, the model has a semi-infinite,
cumulus/stratus-scattering cloud deck and yields $\omega_{0S} =$
0.9967 and $\tau_{AS} = 0.0001$.

Table 4. Observational Mean Values Used in Fitting Models to the Red Spot.

Time (U.T.)	L	R	σ_R	Remarks
				8880 Å
6:18	-56°2	1.70	0.08	
6:35	-45.9	1.72	0.07	
6:46	-39.3	1.72	0.04	Spot's intensity profile unusual
7:01	-30.2	1.57	0.06	
7:19	-19.3	1.50	0.04	
7:29	-13.3	1.52	0.07	Unusually noisy intensity profile
7:46	-3.0	1.55	0.04	
7:56	3.0	1.56	0.03	
8:04	7.9	1.59	0.03	
8:35	26.6	1.55	0.03	
8:58	40.5	1.61	0.01	
9:16	51.4	1.61	0.06	
9:27	58.0	1.74	0.06	
9:35	62.9	(1.53?)	0.08	Affected by seeing and foreshortening
				9215 Å
6:28	-50.2	1.11	0.02	
6:54	-34.5	1.09	0.02	
7:08	-26.0	1.12	0.01	
7:37	-8.5	1.10	0.01	
8:11	12.1	1.08	0.01	
9:09	47.1	1.15	0.01	

measures from repeated trials, from I_1 and I_2 profiles, and in some cases from the two methods. In all cases the formal uncertainty of $R(8880)$ is less than 5%, but as noted in Table 4 there are cases where noise in the Spot profiles could have led to systematic errors.

The value of R gotten from the last 8880 Å profile is highly suspect because the center of the Red Spot was only 2 arc seconds from the terminator. Convolutions of hypothetical Spot/Zone brightness distributions with Gaussian seeing indicate that in this situation seeing is starting to blur the foreshortened Spot so severely that its center appears considerably fainter than it actually is, leading to the measurement of a low R value.

Measurements of our photographs give 8.7 by 4.3 arc seconds for the Spot's dimensions. In the blue the Spot was a perfect oval extending about 25° in longitude and having uniform albedo. At 8880 Å the Spot also appeared to have uniform brightness, but the length derived from analysis of the intensity profiles is only about 7.1 arc seconds. The latter probably indicates that, on the average, the scan line passed through the Spot about 2 degrees in latitude away from its exact center, but considering that the Spot was about 12° wide in the north-south direction, this is not likely to have much effect.

THEORETICAL MODELS

The reflectivity of a given point on Jupiter depends on many factors. First, there are the usual, purely geometric variables related to longitude and latitude which specify how the point is illuminated by the sun and observed from the earth, namely:

$$\mu = \cos\theta = \cos l \cos L \cos D_E + \sin l \sin D_E , \tag{9}$$

$$\mu_0 = \cos\theta_0 = \cos l \cos(L - A_S + A_E) \cos D_S + \sin l \sin D_S, \tag{10}$$

and

$$\phi - \phi_0 = \cos^{-1} \frac{\cos(180° - i) + \mu\mu_0}{[(1 - \mu^2)(1 - \mu_0^2)]^{\frac{1}{2}}}, \quad 0° \leq \phi - \phi_0 \leq 180°, \tag{11}$$

where i is the (absolute) phase angle, (A_E, D_E) and (A_S, D_S) are planetocentric right ascensions and declinations of the earth and sun (available from planetary ephemerides), and the other quantities have their usual meanings (see Appendix). Second, reflectivity is determined by the details of atmospheric structure. The vertical distribution of gas and clouds and the scattering and absorption properties associated with both all interact to produce the observed reflectivity behavior. Our task is to find the simplest structural model capable of reproducing this behavior, a model that it is hoped will reflect the essential features of reality in spite of the simplifications required for theoretical treatment. Toward this end, we shall describe the methods used to compute the scattering properties of homogeneous cloud layers, discuss selection of the

39

scattering phase function, and finally show how reflectivity is computed from structure for the three model types that we have investigated. .

Scattering and Transmission Functions for the Clouds

Any horizontally homogeneous atmosphere, no matter how complex its vertical structure, can be treated as a stack of individually homogeneous layers, each layer being either a scattering/absorbing layer or a purely absorbing layer as may be required. The reflection and transmission properties of the whole stack can be found by "adding" the reflection and transmission properties of all of the constituent layers. For the present, we will confine our attention to finding the properties of homogeneous scattering layers, since this is the first step toward any theoretical model including realistic clouds.

Following the usage of Chandrasekhar (1960), the angular distributions of light diffusely reflected and transmitted by a homogeneous layer are specified by a scattering function (S) and a transmission function (T). These are most generally defined by

$$I_R(\mu,\phi) \;=\; \frac{1}{4\pi\mu} \int_0^{2\pi}\!\!\int_0^1 S(\mu,\phi;\mu',\phi')\, I_i(\mu',\phi')\, d\mu'\, d\phi' \tag{12}$$

$$I_T(\mu,\phi) \;=\; \frac{1}{4\pi\mu} \int_0^{2\pi}\!\!\int_0^1 T(\mu,\phi;\mu',\phi')\, I_i(\mu',\phi')\, d\mu'\, d\phi', \tag{13}$$

where I_i, I_R, and I_T are the incident, reflected, and transmitted specific intensities. In the special case of illumination by a point source in the direction (μ_0,ϕ_0) emitting flux F_0, these reduce to forms that

more clearly reveal the rationale behind the more general definitions:

$$I_R(\mu,\phi) = F_0 S(\mu,\phi;\mu_0,\phi_0)/4\pi\mu \qquad (14)$$

$$I_T(\mu,\phi) = F_0 T(\mu,\phi;\mu_0,\phi_0)/4\pi\mu. \qquad (15)$$

S and T functions can also apply to inhomogeneous layers, but here one must be aware that there are actually two sets of functions, one applying when the illumination is from below and the other when the illumination is from above. When we make subsequent references to S in the context of multilayered models, it is to be understood that illumination is from above. For a homogeneous layer of particles, S and T depend only upon the scattering optical depth of the layer, τ, the single-scattering phase function, $p(\Theta)$, and the single-scattering albedo, ω_0.

We have computed S and T functions using the thin-layer "doubling" method developed by Hansen (1969a). The functions are obtained as azimuth-independent coefficients of Fourier series like

$$S(\mu,\phi;\mu_0,\phi_0) = \sum_{m=0}^{M} S^m(\mu,\mu_0) \cos[m(\phi - \phi_0)], \qquad (16)$$

where m is the order of the coefficient and M depends largely upon the particulars of the phase function considered (M is zero for isotropic scattering). The doubling process is started with a layer of such small optical depth (2^{-25} to 2^{-15}, depending on m) that S and T are known because they arise from single scattering only:

$$S^m(\tau_0;\mu,\mu_0) = \left(\frac{1}{\mu} + \frac{1}{\mu_0}\right)^{-1} \left\{ 1 - \exp\left[-\tau_0\left(\frac{1}{\mu} + \frac{1}{\mu_0}\right)\right]\right\} \omega_0 p_S^m(\mu,\mu_0)$$

$$(17)$$

$$T^m(\tau_0; \mu, \mu_0) = \left(\frac{1}{\mu} - \frac{1}{\mu_0}\right)^{-1}\left[\exp\left(\frac{-\tau_0}{\mu_0}\right) - \exp\left(\frac{-\tau_0}{\mu}\right)\right]\omega_0 p_T^m(\mu, \mu_0)$$

(18)

where

$$p_{S,T}^0(\mu, \mu_0) = \frac{1}{2\pi}\int_0^{2\pi} p(\Theta_{S,T})\,d\phi$$

(19)

and

$$p_{S,T}^m(\mu, \mu_0) = \frac{1}{\pi}\int_0^{2\pi} p(\Theta_{S,T})\cos[m(\phi - \phi_0)]\,d\phi, \quad m \geq 1$$

(20)

with

$$\cos\Theta_{S,T} = \pm\mu\mu_0 + [(1 - \mu^2)(1 - \mu_0^2)]^{\frac{1}{2}}\cos(\phi - \phi_0),$$

(21)

the minus sign being taken for S, the plus sign for T. These initial S^m and T^m are used with Hansen's "doubling" formulae (derived by finding all of the possible pathways for the escape of radiation from the top or bottom of a composite layer formed by two identical layers placed one above the other) to obtain S^m and T^m for $2\tau_0$, then $4\tau_0$, and so on until τ becomes as large as desired. The end results are sets of $S^m(\mu, \mu_0)$ and $T^m(\mu, \mu_0)$ in numerical form as square matrices, each L elements along a side. If S and T are required for optical depths that are not integer powers of 2, they can be obtained by layer "adding," for example, optical depth 2.5 from $2 + \frac{1}{2}$, 5 from $4 + 1$, 7 from $4 + 2 + 1$, and so on.

Application of the doubling method to isotropic scattering $(p(\Theta) = 1)$ is straightforward and yields S and T accurate to about one part in 10^5. For realistic cloud scattering, however, one is forced to deal with strongly anisotropic phase functions (like that in Fig. 11), which often show variations of four or five orders of magnitude over the
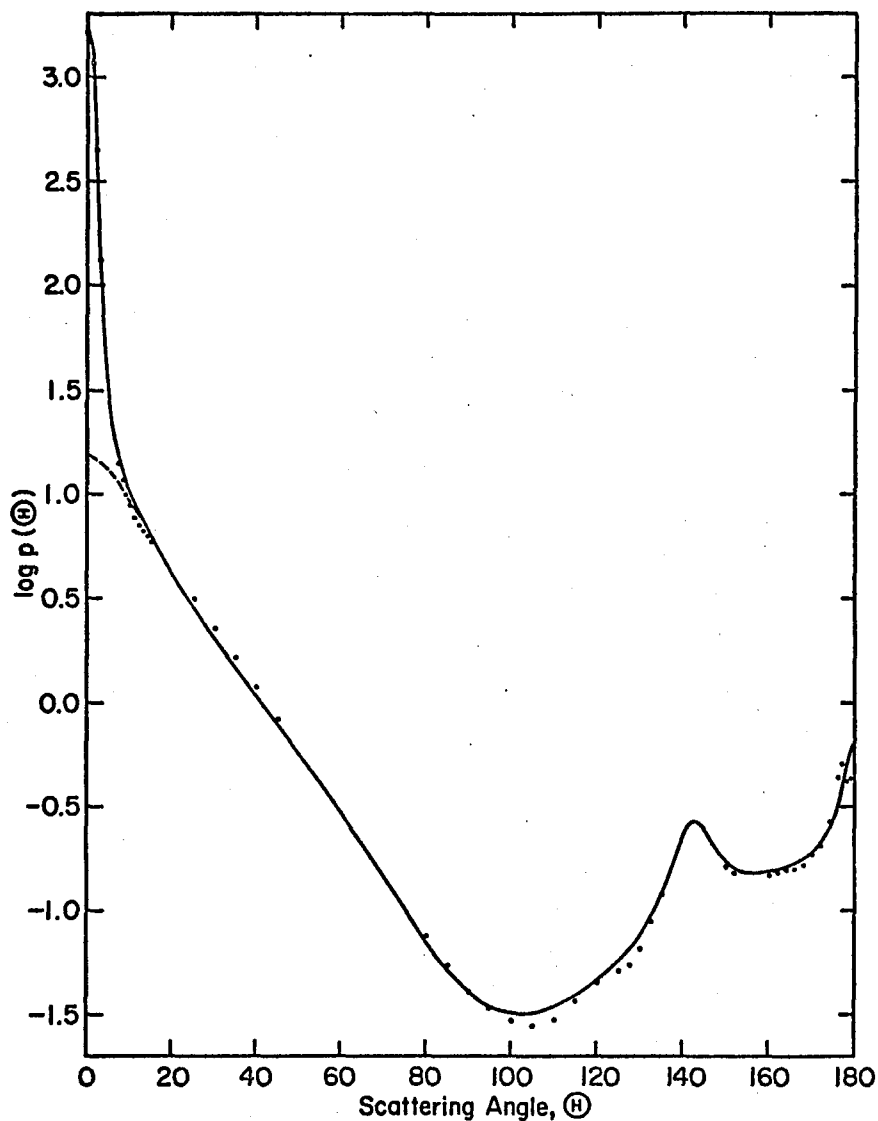
Fig. 11. The Cumulus/Stratus Cloud Phase Function.

The solid curve is the full phase function, including
the forward-scattering peak. Dots are values of the
Deirmendjian phase function (see text) where it dif-
fers by more than 5% from the functional approximation
(solid curve). The dashed curve at small scattering
angles represents the cumulus/stratus phase function
after truncation of the forward-scattering peak.

180° range of scattering angle (Θ), and further, contain sharp features like the forward and backscattering ("glory") peaks. Use of the unmodified doubling method in such cases requires herculean computational effort because, to maintain accuracy of about 1% in the final S and T, 300 to 500 Fourier orders must be doubled with L in the range of 50 to 100 in order to maintain accuracy in the numerical integrations by Gaussian quadrature. To avoid this we have made use of two modifications that greatly reduce M and L requirements while still keeping 1% or 2% accuracy in S and T.

The first of these is the forward-peak truncation (or delta function) approximation described by Hansen (1969b), by Potter (1970), and by Hansen and Pollack (1970). Photons scattered through small angles (Θ ≤ 10°) are treated as if they had not been scattered at all. In practice this approximation is made by removing the forward peak from the phase function (as in Fig. 11) to obtain the truncated function, $p_{TR}(\Theta)$, then by using the new variables

$$p'(\Theta) = p_{TR}(\Theta)/x \tag{22}$$

$$\tau' = x\tau \tag{23}$$

$$\omega_0' = [1 + (1 - \omega_0)/x\omega_0]^{-1} \tag{24}$$

(where x is the integral of $p_{TR}(\Theta)$ over solid angle) in place of $p(\Theta)$, τ, ω_0 in the doubling process. Since this modification in effect makes the phase function less anisotropic and removes one of the sharp features, both M and L can be substantially reduced.

The second modification used is the renormalization approximation of Hansen (1971), which slightly modifies the initial $T^m(\mu,\mu_0)$

matrices on the basis of the phase function so that L can be reduced by at least half without reducing the Gaussian quadrature accuracy. Since computational effort increases approximately as L^3, this represents an important saving. The two modifications together reduce the doubling requirements for the phase function of Fig. 11 to $M = 50$ and $L = 11$.

The Cumulus/Stratus Phase Function

The light-scattering properties of the Jovian cloud particles are as yet unknown. Little information is available on which to base selection of a phase function, mainly because the 0° to 12° range of phase angle observable from earth is too small to allow inference of the phase function from phase-angle variations of polarization and bright- ness. Lewis (1969) applied the chemical thermodynamics of the NH_3/H_2O system to Jupiter's atmosphere and concluded that the uppermost clouds must be nearly pure solid NH_3 and the lower-level clouds solid and liq- uid solutions of NH_3 in H_2O with some ammonium hydrogen sulfide. On the basis of the similar physical properties of NH_3 and H_2O, particularly with respect to refractive index, dielectric constant, heat of vaporiza- tion, etc., we speculate that Jovian clouds are similar to terrestrial ice and water clouds with respect to optical properties and average par- ticle size.

Granted this premise, the logical first choice for a phase func- tion to represent the upper clouds of Jupiter would be one applying to terrestrial cirroform clouds composed of ice particles. Unfortunately, such is not yet available, even from theory (because of the difficulty of obtaining solutions from electromagnetic theory for scattering by

complex crystalline shapes). If the ice particles are spherical, it is likely that the phase function is generally similar to that of equivalent water droplets. Hansen and Pollack (1970) have successfully reproduced reflectivity measurements made on thick cirrus using spherical ice particles of about 20 μm in radius, for example. However, if the particles depart much from spherical shape (as is likely the case if they form by direct condensation from the vapor phase), then features seen in water droplet phase functions (like the glory and rainbows) may be diminished or absent, and new features resulting from the particulars of crystalline geometry might appear (Coffeen and Hansen, 1973).

The phase function we have chosen (Fig. 11, Table 5) is a water-cloud phase function. It is a close approximation to the cumulus cloud phase function of Table T.36 of Deirmendjian (1969), the latter computed using a purely real refractive index of 1.33 and a modified gamma distribution of droplet sizes with modal radius equal to 4.0 μm. This phase function is very similar to the "typical" cloud function used by Hansen (1969b), and is not much different from the fair-weather cumulus, altostratus, and stratus phase functions for wavelength 1.2 μm shown in Hansen (1971). The asymmetry parameter

$$g = \frac{1}{2} \int_0^\pi p(\Theta) \cos\Theta \sin\Theta \, d\Theta \qquad (25)$$

is 0.850, a value typical of strongly forward-scattering large particles with refractive index near 1.33.

The function used to approximate the Deirmendjian phase function is given in Table 5. This function contains terms of two types (aside from the constant term), which are immediately represented as Fourier

series; that is, the Fourier-coefficient integrals of Eqs. (19) and (20) are known as explicit functions of m, μ, and μ_0, and so need not be found by numerical methods. This is advantageous for doubling because it simplifies and speeds up the initialization process. The approximate nature of the phase function is not a disadvantage in situations like the present one, where we are interested in typical behavior rather than in specifics.

Table 5. Functions Representing the Full and Truncated Cumulus/Stratus Phase Functions.

$$p(\Theta) \; = \; c_0 + \sum_{i=1}^{3} \frac{c_i(1 - t_i^2)}{1 - 2t_i \cos\Theta + t_i^2} + \sum_{i=4}^{6} \frac{c_i}{1 + t_i(\cos\Theta_i - \cos\Theta)^2}$$

i	c_i	t_i	$\cos\Theta_i$
0	-0.250	--	--
1	1.70	0.80	--
2	0.107	-0.40	--
3	0.01223	-0.95	--
4	-0.243	2.00	0.50000
5	0.190	295.0	-0.79335
6*	1577.1	7.7×10^6	1.00000

*Term No. 6 (representing the forward-scattering peak) is omitted from the truncated phase function, $p_{TR}(\Theta)$.

48

The Reflectivity of Structural Models

We have investigated three simple structures proposed for the
Jovian atmosphere to account for various spectroscopic observations: (1)
the semi-infinite scattering model, (2) the reflecting layer model, and
(3) the two-layer cloud model of Danielson and Tomasko (1969). These
types are shown and compared in Fig. 12.
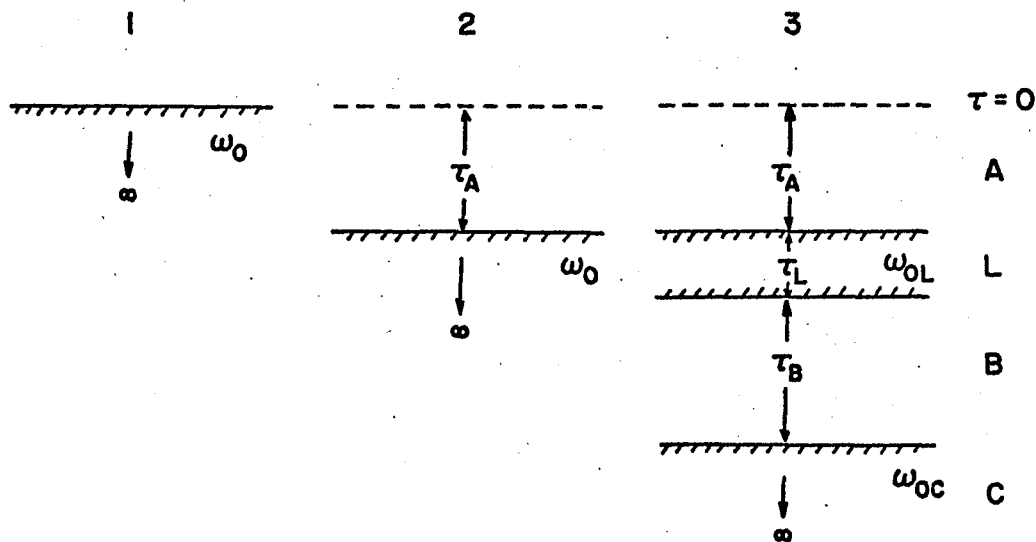
Fig. 12. Schematic Vertical Structures for the Theoretical Models.

The structures shown are (1) the semi-infinite scatter-
ing model, (2) the reflecting layer model, and (3) the
two-layer cloud model.

The semi-infinite scattering model is the simplest of the three. Its reflectivity is given by

$$G(L, l) = S(\mu, \mu_0, \phi - \phi_0)/4\mu, \tag{26}$$

where S is the scattering function for a homogeneous, semi-infinite scattering atmosphere. Aside from the choice of phase function, the model has only one free parameter, ω_0. No models of this kind with either isotropic or cumulus/stratus scattering were found that even came close to reproducing our 8880 Å observations. In every case, when any value of ω_0 was found that would make the model fit at the central meridian point of the observational limb-darkening curve, the model was too bright at other longitudes. The reflectivity of the models still decreases toward the limbs, but at a much slower rate than the observed reflectivity.

Some practical considerations enter into the computation of S for a particular set of μ, μ_0, and $\phi - \phi_0$ values. For isotropic scattering S is obtained from doubling as the $L \times L$ square matrix $S^0(\mu, \mu_0)$, so S for a particular μ and μ_0 can be found by interpolation first with respect to μ, then with respect to μ_0, using the Lagrange method. For forward scattering we have $M\, S^m(\mu, \mu_0)$ matrices, and $\phi - \phi_0$ enters the picture. The most accurate and economical way to proceed is to first form the Fourier series for the particular value of $\phi - \phi_0$ and all L^2 elements of the matrices so as to obtain the matrix $S(\mu, \mu_0)$, then interpolate for the desired μ and μ_0 in this matrix.

A problem arises when the phase function has a sharp backscattering lobe and the cloud surface is observed at phase angles smaller

than about 10°. In this case, $\mu \simeq \mu_0$ and $\phi - \phi_0 \simeq 180°$ and we find that

the $S(\mu,\mu_0)$ matrix formed has elements that rapidly increase near the

diagonal, leading to poor results when Lagrange interpolation is used.

Instead, we have interpolated for near-diagonal values of μ and μ_0 by

fitting the function for single scattering,

$$S(\mu,\mu_0,\phi - \phi_0) = \left(\frac{1}{\mu} + \frac{1}{\mu_0}\right)^{-1}\left\{1 - \exp\left[-\tau\left(\frac{1}{\mu} +\frac{1}{\mu_0}\right)\right]\right\}\omega_0 p(\Theta_S),$$

(27)

to matrix elements lying on or immediately adjacent to the diagonal.

The reflectivity of the reflecting layer model is given by

$$G(L,l) = e^{-\tau_A X(\mu_0)} e^{-\tau_A X(\mu)} S(\mu,\mu_0,\phi - \phi_0)/4\mu,$$

(28)

where $X(\mu_0)$ and $X(\mu)$ are the effective air masses for entrance and exit

paths through an absorbing gas layer of optical depth τ_A, and S is the

scattering function for the semi-infinite cloud which serves as the re-

flecting layer. In general there are two free parameters (aside from

the choice of phase function), τ_A and ω_0. We have been able to fit our

observations at both wavelengths with such two-parameter models; results

will be described later. For the present we are concerned with the more

usual form of the reflecting layer model where the cloud surface serves

only as a reflector and contributes only as much to the total absorption

at the band wavelength as it absorbs by itself at continuum wavelengths.

In this case ω_0 is no longer a free parameter; it is fixed at the value

found by fitting the 9215 Å observations.

In the general case the effective air mass, $X(\mu)$, is a line in-

tegral over the optical path and includes curve-of-growth behavior for

the particular absorption band of interest. We have considered two sim-
plified extremes for the CH_4 8873 Å band. In the first case it is as-
sumed that the band is "weak" in the sense that all absorption occurs on
the linear part of the curve of growth; then absorption strength is
directly proportional to the path length through the methane layer,
leading to

$$X(\mu) = 1/\mu. \tag{29}$$

At the other extreme, the band is assumed to be fully saturated, with
absorption strength proportional to the square root of the path length:

$$X(\mu) = \sqrt{1/\mu}. \tag{30}$$

Single-parameter reflecting layer models with linear or satu-
rated CH_4 absorption and isotropic or cumulus/stratus scattering were
compared with the 8880 Å observations, but none even came close to re-
producing them. The sense of the deviations from the observational
limb-darkening curve is opposite to that found in the case of the
semi-infinite scattering models. When τ_A is adjusted so that the model
correctly reproduces the observed central-meridian reflectivity, the
model reflectivity decreases far too rapidly toward the limbs. In view
of the rather large values of τ_A required (0.83 for the South Tropical
Zone), such behavior is not surprising.

The two-layer cloud model (No. 3 in Fig. 12) actually consists
of four layers, an upper and a lower cloud layer (labeled L and C, re-
spectively), and an upper and a lower layer of purely absorbing gas (A
and B). (In the wavelength region we are considering, Rayleigh

scattering by the gas is negligible.) Reflectivity is computed from equations similar in form and derivation to the layer "adding" formulae previously mentioned:

$$G(L, \mathcal{Z}) \;=\; \frac{1}{4\mu} \sum_{m=0}^{M} S^m(\mu, \mu_0)\, \cos[m(\phi - \phi_0)] \tag{31}$$

$$
\begin{aligned}
S^m(\mu,\mu_0) \;=\; & e^{-\tau_A X(\mu)}\, e^{-\tau_A X(\mu_0)} \Big\{ S_L^m(\mu,\mu_0) \\[6pt]
& + e^{-\tau_L/\mu_0}\, e^{-\tau_B X(\mu_0)}\, e^{-\tau_L/\mu}\, e^{-\tau_B X(\mu)}\, \textstyle\sum_0^m(\mu,\mu_0) \\[6pt]
& + e^{-\tau_L/\mu_0}\, e^{-\tau_B X(\mu_0)}\, C \int_0^1 T_L^m(\mu,\mu') \\[6pt]
& \qquad\qquad \cdot\; e^{-\tau_B X(\mu')}\, \textstyle\sum_0^m(\mu',\mu_0)\dfrac{d\mu'}{\mu'} \\[6pt]
& + e^{-\tau_L/\mu}\, e^{-\tau_B X(\mu)}\, C \int_0^1 \textstyle\sum_0^m(\mu,\mu')\, e^{-\tau_B X(\mu')} \\[6pt]
& \qquad\qquad \cdot\; T_L^m(\mu',\mu_0)\, \dfrac{d\mu'}{\mu'} \\[6pt]
& + C \int_0^1 T_L^m(\mu,\mu')\, e^{-\tau_B X(\mu')} \left[C \int_0^1 \textstyle\sum_0^m(\mu',\mu'') \right. \\[6pt]
& \qquad\qquad \left. \cdot\; e^{-\tau_B X(\mu'')}\, T_L^m(\mu'',\mu_0)\, \dfrac{d\mu''}{\mu''} \right] \dfrac{d\mu'}{\mu'} \Big\}\;,
\end{aligned}
\tag{32}
$$

where

$$C \;=\; \begin{cases} \tfrac{1}{2} & \text{if } m = 0 \\[6pt] \tfrac{1}{4} & \text{if } m \geq 1 \end{cases} \tag{33}$$

$$\textstyle\sum_0^m(\mu,\mu_0) \;=\; S_1^m(\mu,\mu_0) + S_3^m(\mu,\mu_0) + S_5^m(\mu,\mu_0) + \dots \tag{34}$$

and $\quad S_1^m (\mu,\mu_0) \quad = \quad S_C^m (\mu,\mu_0)$

$$S_2^m (\mu,\mu_0) \quad = \quad C \int_0^1 S_L^m (\mu,\mu') \; e^{-\tau_B X(\mu')} \; S_1(\mu',\mu_0) \; \frac{d\mu'}{\mu'}$$

$$S_3^m (\mu,\mu_0) \quad = \quad C \int_0^1 S_C^m (\mu,\mu') \; e^{-\tau_B X(\mu')} \; S_2(\mu',\mu_0) \; \frac{d\mu'}{\mu'}$$

$$S_4^m (\mu,\mu_0) \quad = \quad C \int_0^1 S_L^m (\mu,\mu') \; e^{-\tau_B X(\mu')} \; S_3(\mu',\mu_0) \; \frac{d\mu'}{\mu'}$$

$$S_5^m (\mu,\mu_0) \quad = \quad C \int_0^1 S_C^m (\mu,\mu') \; e^{-\tau_B X(\mu')} \; S_4(\mu',\mu_0) \; \frac{d\mu'}{\mu'}$$

etc. (35)

The S^m of Eqs. (31) and (32) refers to the scattering function of the whole multilayered structure, S_L^m and T_L^m are scattering and transmission functions for the upper cloud layer, and S_C^m is the scattering function for the lower cloud. The S_n^m integrals apply to radiation diffusely reflected up and down between the cloud layers, n being the number of reflections. For n greater than 5 or 6, the ratio $R = S_n^m/S_{n-1}^m$ becomes constant, allowing termination of the series of Eq. (34) by adding the single term $S_7^m/(1-R^2)$. $X(\mu)$ is again the effective air mass, in our models given by either Eq. (29) or Eq. (30).

Since the two-layer cloud models have five free parameters (τ_A, τ_B, τ_L, ω_{0L}, and ω_{0C}), it is not surprising that they can fit our observations. We have found whole series of models whose parameters vary continuously over limited ranges that reproduce the 8880 Å limb-darkening curves. "Unique" model fits are obtained only when the 9215 Å observations are used to fix ω_0. In the next two sections we shall discuss these model fits in some detail, touching upon methods of fitting, giving

results in organized form so that trends of behavior are apparent, and looking for similarities and differences among the three regions of Jupiter and between the results obtained by making different kinds of assumptions as to cloud scattering and methane absorption.

MODELS WITH ISOTROPIC SCATTERING

Until the recent introduction of practical techniques like the thin-layer doubling method, it was difficult and costly to compute the reflection and transmission of layers composed of particles having any desired phase function. The usual procedure in the treatment of light scattering by clouds was to assume isotropic scattering because this was one of the few simple cases where general solutions had been found by Chandrasekhar (1960), making it possible to compute scattering and transmission functions for particular layers without much computational effort. Isotropic scattering is quite unrealistic for terrestrial clouds, of course, but there is one advantage (aside from computational simplicity) associated with it. The transformation equations of van de Hulst and Grossman (1968) allow τ and ω_0 parameters applying to an isotropic scattering layer to be scaled to τ' and ω_0' parameters that apply to an approximately equivalent anisotropic layer. For example, these transformations have been used by Danielson and Tomasko (1969) to find the thickness of the upper cloud layer of their model in the case where the cloud particles scatter strongly in the forward direction as do terrestrial cloud particles, and to determine the higher single-scattering albedo necessarily associated with such particles.

We have undertaken the fitting of our observations with models assuming isotropic scattering for several reasons. First, only isotropic results are available from previous work, requiring us to consider isotropic models in order to be able to make direct comparisons. Second,

55

our isotropic results can be compared with our corresponding results based on cumulus/stratus cloud scattering to yield some understanding of the effects of making a drastic change in the nature of the phase function. Here we are interested particularly in testing the accuracy of van de Hulst-Grossman scaling in a specific case typical of those encountered in studying the outer planets. Finally, since it will be shown that isotropic and forward-scattering models often show parallel trends of behavior when certain parameters are varied, these trends can be fully explored with the minimum computational expense by making investigations with isotropic models only.

The first step in the interpretation of the observations is the determination of the continuum single-scattering albedo by means of fitting models to the 9215 Å limb-darkening curves. This albedo specifies the amount of absorption attributable to the cloud particles themselves as distinguished from absorption due to the methane gas in which the particles are distributed, so it will serve as the upper limit of the ω_0 values considered in fitting the 8880 Å observations with models.

If the spectral region passed by the 9215 Å filter could be safely considered to be rigorously pure continuum, then the model used to fit the observed limb darkening would simply be a semi-infinite scattering atmosphere. However, the passband is almost certainly contaminated by a number of weak methane and ammonia lines. To allow for this additional absorption, the model we have used consists of a layer of absorbing gas overlying a semi-infinite cloud deck. The optical depth of the absorbing layer ought to be small if the 9215 Å region is actually close to being continuum. The results of fitting two-parameter models

to the observations of the three Jupiter regions (see Table 6) show that this is indeed found to be the case. The somewhat larger value of τ_A found for the North Polar Region may not be significant because of the poorer quality of the observations in this instance, or more likely, because observations lying outside of longitudes -45° and +45° were not included on account of the effects of seeing, and it is the near-limb observations that weigh most heavily in determining the values of the derived τ_A that are missing in this case. For the same reasons, the ω_0 value found for the North Polar Region is also somewhat suspect. The true value is probably smaller than the best-fit value of Table 6, which is very nearly the same as the best-fit value for the South Tropical Zone. This latter coincidence of values is unlikely because it implies that the N.P.R. and the Zone should appear to have about the same albedo at continuum wavelengths, whereas the N.P.R. appeared to be the darker region both visually and photographically.

The ω_0 derived for the South Tropical Zone, 0.987-0.989, lies well within the approximate range 0.94-0.993 indicated for 9200 Å by Axel's (1972) graphical summarization of the observational evidence. The fact that our value lies more toward the high end of Axel's range is not surprising for two reasons: (1) Our blue-light photos of Jupiter made coincidentally with our scanner observations show that the South Tropical Zone was the brightest large feature on the planet at this time, and (2) the lower limit of about 0.94 is derived from Taylor's (1965) spectrophotometry of Jupiter's whole disk, so it represents a weighted average of the belts and zones rather than a bright feature like the South Tropical Zone. The issue is further complicated

by the possibility of significant time variations of albedo both for individual features and for the planet considered as a whole. The somewhat higher ω_0 found for the Red Spot is a consequence of the observation that it is slightly but definitely brighter than the surrounding South Tropical Zone at 9215 Å.

Table 6. Isotropic-Scattering Models Fitted to the 9215 Å Observations (Giving Best Fits and Approximate Limiting Cases Found).

Region	ω_0	τ_A	$\sigma \times 10^2$	Remarks
South Tropical Zone	0.9866	0	1.28	Model is too bright near the limb and terminator
	0.9873	0.004	1.00	Exact fit at longitudes -45°, 0°, and +45°
	0.9880	0.009	0.84	Best over-all fit to the observations
	0.9890	0.016	1.04	Model is too faint at longitudes ±10 to 40°
North Polar Region	0.981	0.06	1.6	Model is too bright near longitudes -45° and +45°
	0.9874	0.074	0.39	Best over-all fit to the observations
	0.993	0.09	1.5	Model is too faint near longitudes -45° and +45°
Red Spot	0.9928	0	--	Approximately the best fit to the observations
	0.995	0.02	--	Model is too faint near the limb and terminator

As a prelude to the discussion of fitting the 8880 Å observations with models, it is necessary to consider how the properties of a scattering layer are changed when an absorbing gas is present between the particles. If the scattering optical depth of the layer is large enough that most of the diffusely reflected and transmitted photons have been multiply-scattered within the layer, then the effect of the gas is to reduce ω_0 from the value ω_0^* that would apply if there were no gas present approximately according to

$$\omega_0 = \omega_0^* \exp(-l_s/l_a), \qquad l_a > l_s, \qquad (36)$$

where l_s and l_a are respectively the scattering and gas-absorption mean free paths. To decrease ω_0 is, in effect, to distribute the scattering particles more sparsely in the gas matrix, increasing the probability that photons will be absorbed between successive scatterings. The possibilities range from the case where the cloud is so compact that ω_0 is only slightly smaller than ω_0^*, to the case where the cloud is actually a very thin haze in which gas absorption so dominates scattering that the "cloud" layer behaves much as if it were purely absorbing gas.

The upper limit to ω_0 is, of course, the value derived from the 9215 Å observations as previously described. Let us consider the possible existence of a practical lower limit where the implausible very thin haze is encountered. On the earth, scattering mean free paths are on the order of 10 to 100 m for the cumulus or stratus cloud types whereas much longer paths, on the order of a kilometer or more, occur for light fog, smog, and natural aerosol hazes. So let us somewhat arbitrarily take $l_s = 10$ km to represent the very-thin-haze limit. We can compute a

value of ω_0 corresponding to this limit if l_a, the absorption mean free path at the upper-cloud level of Jupiter's atmosphere, can be determined. This value depends upon the local density of methane, ρ, and upon the mass absorption coefficient for the 8880 Å band, κ:

$$l_a = 1/\kappa\rho. \qquad (37)$$

An approximate value of ρ for the upper-cloud level can readily be obtained from published atmospheric models--for example, Model I(130) of Savage and Danielson (1968) yields $\rho \simeq 8 \times 10^{-7}$ gm/cm^3 for the 145°K level--but the value of κ is not yet accurately known from laboratory measurements of the 8880 Å band. However, we can derive a rough estimate of κ from the following considerations. Our observations show that the central regions of Jupiter's disk are about 0.18 times as bright at 8880 Å as at 9215 Å, indicating a $\tau \simeq 0.85$ for all absorption due to methane. We would like to know the abundance of methane giving rise to the observed degree of extinction, but this is complicated by the fact that the partial transmission of the upper cloud layer reduces the effectiveness of the methane below this level in comparison to that above it. Consider the extreme case where the upper cloud is so opaque that all of the observed extinction can be attributed to the methane above the clouds (20 meter-amagats according to Table 1 of Danielson and Tomasko, 1969). This leads to an upper limit $\kappa \simeq 0.6$ cm^2/gm. At the other extreme, where the upper cloud has negligible effect, we attribute the observed absorption to all of the methane above the *lower* cloudtops (67 m-amagats), leading to a lower limit $\kappa \simeq 0.2$ cm^2/gm. The intermediate value, $\kappa \simeq 0.4$ cm^2/gm, seems most realistic. It yields $l_a \simeq 30$ km and

indicates that the very-thin-haze limit occurs at about $\omega_0 = 0.7$ (approximate range 0.6 to 0.85).

Fitting of the 8880 Å observations with two-layer cloud models of the kind proposed by Danielson and Tomasko (1969) confronts one with the problem of dealing with the numerous model parameters. In addition to the uncertainty as to the scattering phase function of the cloud layers and the uncertainty concerning the degree of saturation in the 8880 Å band, the completely general model contains the five free parameters τ_A, τ_B, τ_L, ω_{0L}, and ω_{0C}. To consider all possibilities for all of these variables would be an impractical and unnecessary task. At the outset it seemed reasonable to suppose that the upper and lower cloud layers are not greatly dissimilar in terms of particle characteristics and number densities and to set $\omega_{0L} = \omega_{0C}$, dealing with ω_0 as an independent variable within the limits previously discussed. This latter seemed justified by the finding of Danielson and Tomasko that the upper cloud is thick enough ($\tau \simeq 2$ for isotropic scattering) to ensure the dominance of multiple scattering and hence the validity of Eq. (36) for the upper layer, as well as for the semi-infinite lower cloud.

Our models of this kind (Table 7, Fig. 13) indicate a thinner upper layer than was expected, making questionable the assumption of dominance of multiple scattering. In particular, the optical thickness of about 0.7 found in the case of models with linear CH_4 absorption implies that only about half of the photons incident upon the upper cloud are scattered *at all* and that the multiple-scattering contribution is correspondingly minor (for near-normal angles of incidence and reflection/transmission). Because of this result we investigated a

second type of model more appropriate to the case of a thin upper cloud layer. In this case it is assumed that the reflected and transmitted light arises predominantly from single scattering and that gas and particle absorptions are "decoupled," that is, the photons scattered behave as if they have seen particles having $\omega_{0L} = \omega_0{}^*$, and absorption due to interparticular gas (presumably small on account of the thinness of the layer) can be attributed to the A and/or B gas layers. Hence ω_0 for the upper cloud is fixed at the value derived from the 9215 Å observations, whereas the ω_0 for the lower cloud is treated as the independent parameter of the model.

Table 7. Two-Layer, Isotropic-Scattering Models That Best Fit the 8880 Å Observations of the South Tropical Zone.

ω_0	Linear CH4 absorption				Saturated CH4 absorption			
	τ_A	τ_L	τ_B	$\sigma \times 10^2$	τ_A	τ_L	τ_B	$\sigma \times 10^2$
0.9873	0.300	0.71	1.03	1.03	0.525	1.40	1.25	0.60
0.95	0.286	0.73	0.82	0.88	0.499	1.61	1.6	0.56
0.90	0.269	0.78	0.63	0.84	0.455	1.90	∞[a]	0.63
0.85	0.253	0.85	0.47	0.77	0.406	2.33	∞[a]	0.96
0.8075	--	--	--	--	0.370	∞	∞	1.28
0.80	0.235	0.95	0.32	0.72	--	--	--	--
0.75	0.217	1.2	0.2	0.69	--	--	--	--
0.6995	0.191	∞	0	0.74	--	--	--	--

[a] In these cases ∞ signifies a large but indeterminate optical depth.

Fig. 13. Layer Thicknesses and Boundary Depths vs ω_0 for the Isotropic-Scattering Models of the South Tropical Zone Having the Same ω_0 for Both Cloud Layers.

Curves for the models assuming saturated CH_4 absorption are shown on the right side of the figure; curves for linear absorption are shown on the left. Upper and lower methane layers are marked A and B, respectively; upper and lower cloud layers are marked L and C.

Models of this second kind were computed for the linear-absorption case (where the thinnest upper layers were indicated). Comparison of these results (Table 8, Fig. 14) with the corresponding results from the first type of model indicates that the most significant difference is that the upper-cloud optical depth decreases with decreasing ω_0 in the former case, but increases in the latter. Even so, the τ_L values do not diverge greatly except for $\omega_0 < 0.8$ where, as we have indicated, the clouds become thinly dispersed haze. In any case, these two series of models clearly show that the effects of different assumptions about upper-layer ω_0 are minor compared to the effects of assuming saturated rather than linear CH_4 absorption. Therefore, we considered it suffi-cient to restrict ourselves to the first type of model in subsequent work.

Model results will generally be presented as in Table 7, where parameters are given only for the best-fitting models found for each value of ω_0. It is to be understood that in every case there exists a range of models, having τ_A, τ_B, and τ_L similar to the given values, which also fit the observations. To illustrate this for a typical case we have included the limits of these ranges of uncertainty in Table 8 and Fig. 14. It should be emphasized that these are ranges of uncer-tainty in derived parameters arising from *observational* uncertainties, and are quite distinct from uncertainties arising from the question of which set of model assumptions is the most realistic. The location of such limits is naturally dependent on the precise meaning of the word "fit." Our usage requires that, if a model fits the observations, then at all points in longitude (L) along the limb-darkening curve the model

Table 8. Two-Layer, Isotropic-Scattering Models Fitted to the 8880 Å Observations of the South Tropical Zone Assuming Linear CH_4 Absorption and Upper-Cloud ω_0 of 0.9873 (with Best Fits and Approximate Limiting Cases Found).

ω_0	τ_A	τ_L	τ_B	$\sigma \times 10^2$	Remarks*
0.9873	0.284	0.65	0.97	1.21	a
	0.300	0.71	1.03	1.03	B
	0.309	0.75	1.09	1.13	c
0.95	0.273	0.60	0.76	1.24	a
	0.292	0.67	0.82	0.89	B
	0.312	0.75	0.94	1.18	c
0.90	0.261	0.54	0.59	1.32	a,b
	0.289	0.64	0.66	0.88	B
	0.308	0.72	0.75	1.09	c
0.85	0.250	0.48	0.44	1.37	a,b
	0.286	0.61	0.53	0.85	B
	0.306	0.70	0.62	1.07	c
0.80	0.240	0.42	0.32	1.30	b
	0.284	0.58	0.41	0.76	B
	0.305	0.68	0.51	1.05	c
0.75	0.210	0.28	0.19	1.29	b
	0.276	0.52	0.28	0.73	B
	0.299	0.63	0.37	0.95	c
0.70	0.190	0	0	0.77	d
	0.258	0.36	0.11	0.63	B
	0.298	0.60	0.26	1.02	c
0.677	0.250	0.26	0	0.60	B,d

*B = best-fitting model for the given value of lower
  cloud albedo, ω_0
a = model is too faint in the region of longitudes
  ±20-30°
b = model is too bright near the limb and terminator
c = model is too faint near the limb and terminator
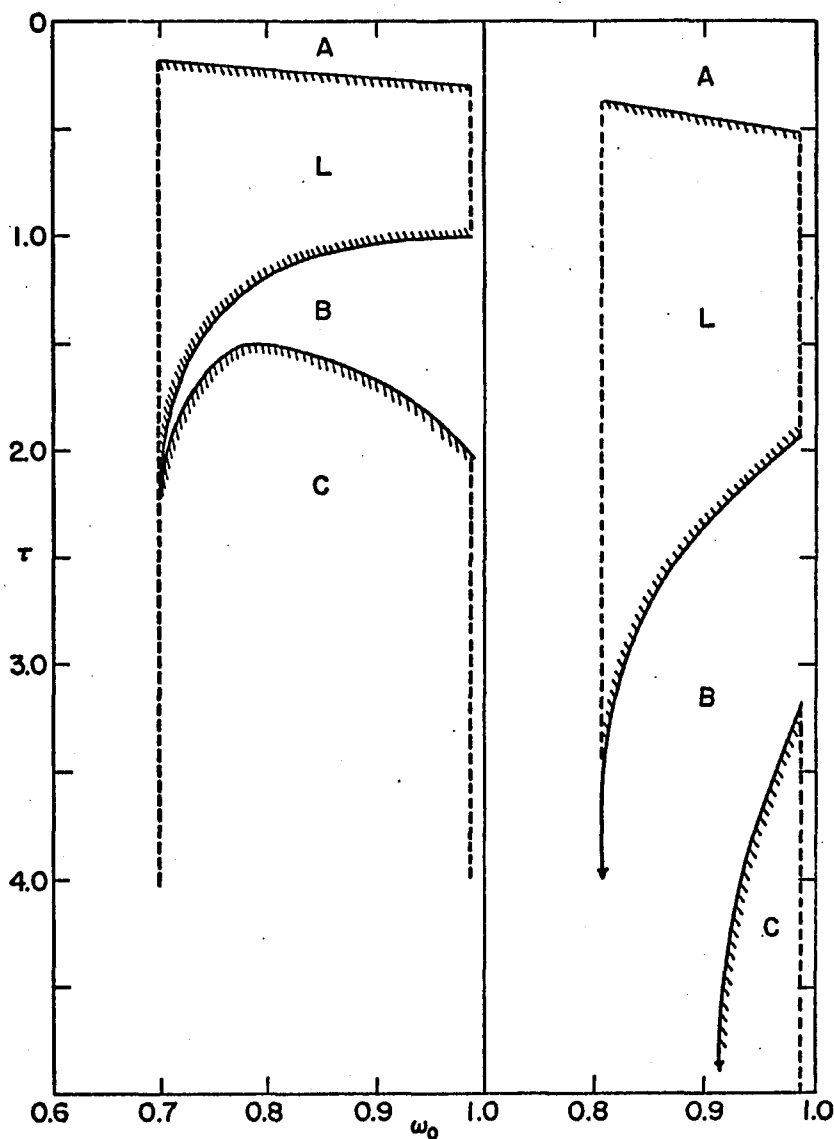d = physical limit of one or more parameters of the
  model
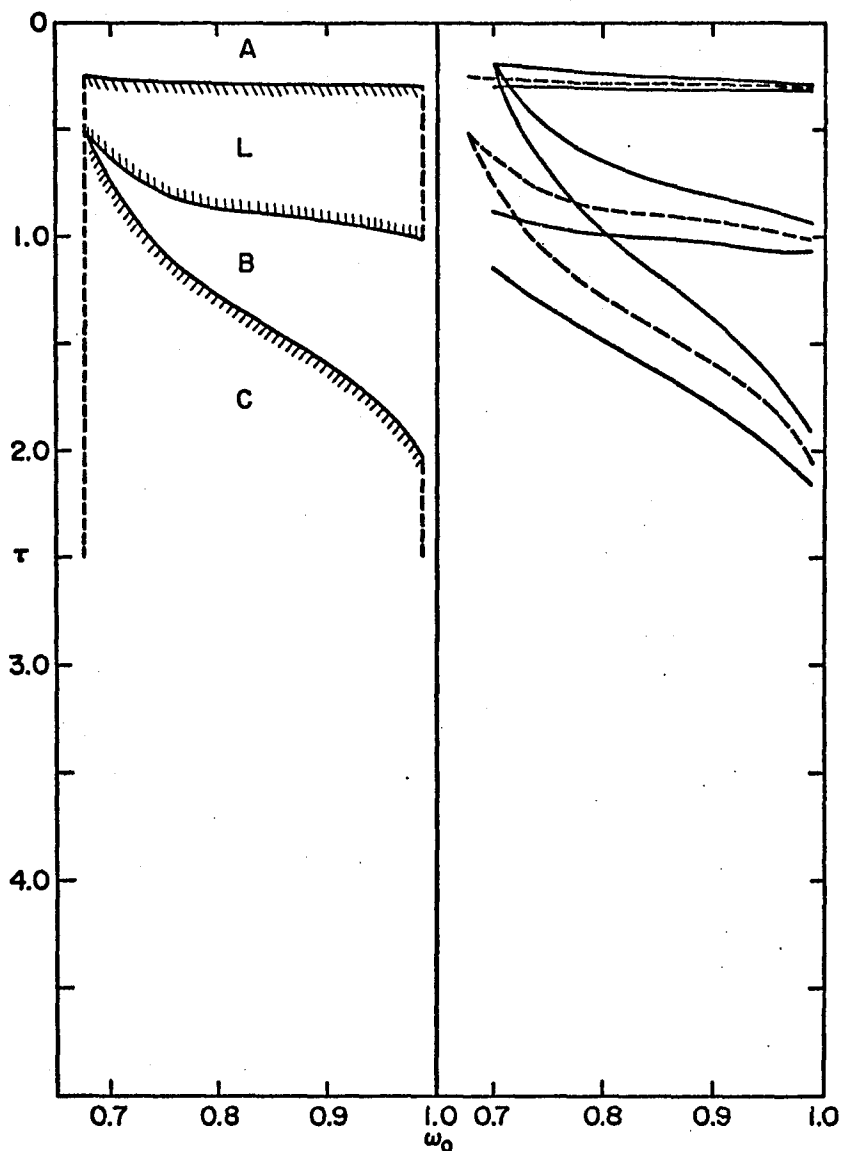
Fig. 14. Layer Thicknesses and Boundary Depths vs ω_0 for the
Isotropic-Scattering Models of the South Tropical Zone
Having Fixed ω_0 for the Upper Cloud Layer.

Curves for the models assuming linear CH_4 absorption are
shown on the left side of the figure. On the right, the
boundaries for the same models are shown as broken lines;
the ranges of uncertainty in the boundary locations that
arise solely from uncertainty in the observations are in-
dicated by solid lines flanking each boundary curve.

value cannot differ from the observational mean by more than $2\sigma_0(L)$,
where $\sigma_0(L)$ is the (somewhat approximate) standard deviation character-
izing uncertainty in the observational mean. We consider this defini-
tion to be somewhat overgenerous in that it occasionally admits fits
that show small but definite systematic departures beyond the apparent
limits allowed by scatter in the observations. Consequently, the limits
indicated in Table 8 and Fig. 14 are probably conservative.

It will be noted from Table 8 that, as one moves through the
range of fitting models (for a given ω_0) from one limit to the other,
the three optical depth parameters are all changing simultaneously. This
derives from the procedure used to locate models capable of fitting the
observations, which it is appropriate to review at this point. First,
having selected a value of ω_0, we compute a number of models, each with
a different τ_L. For each of these models τ_A and τ_B are adjusted (if
physically possible) so that the model limb-darkening curve is con-
strained to intersect the observational curve at longitudes -45°, 0°,
and +45°. Usually (but not always) a model fitting at these three points
at least comes close to fitting at other points as well. We have used
the quantity σ as a generally reliable indicator of the closeness of the
over-all match between model and observations. It is the standard devi-
ation of residuals (observational mean minus model value) at 13 approxi-
mately equally spaced longitudes on the interval $-60° \leq L \leq 60°$. The
"best fitting model" is located by plotting σ against τ_L and noting the
value for which σ is a minimum. (This minimum is clearly distinguisha-
ble except when τ_L is large and/or ω_0 approaches the lower end of its
range.) In most cases σ for the best-fit model is considerably smaller

than $\overline{\sigma_0}$, the average of $\sigma_0(L)$ over all longitudes considered, which serves as an approximate indicator of the over-all uncertainty in the observed limb-darkening ($\overline{\sigma_0} \simeq 1.2 \times 10^{-2}$ for the 8880 Å observations of the South Tropical Zone).

Although our 8880 Å observations of the North Polar Region are considerably noisier than those for the South Tropical Zone, they indicate clearly that, although the limb-darkening curves of the two regions are similar in shape, the North Polar Region is at all points about one third as bright. This result was surprising because the findings of Gehrels, Herman, and Owen (1969) suggest that the polar regions are areas where the clear atmosphere is unusually deep, possibly because the upper NH_3 clouds are absent. If this latter were strictly true, then at 8880 Å one would expect to observe not only greater extinction due to methane absorption but also a steeper limb-darkening curve, one where the brightness drops much more rapidly going toward limb or terminator because there is no contribution to the scattered light due to diffuse reflection from the upper cloud.

To investigate these possibilities, a series of models (Table 9, Fig. 15) were fitted to the observations of the North Polar Region using the same approach as for the South Tropical Zone models of Table 7 and Fig. 13. Models having ω_0 well below the thin-haze "limit" were computed in order to determine whether the observations could be fitted by *any* model having no upper cloud layer. Such models were found (they are the last listed in Table 9), but their ω_0 values require scattering mean free paths much greater than 10 km. On the other hand, two-layer models with *very thin* upper cloud layers and $\omega_0 \simeq \omega_0^*$ avoid this difficulty and are

very good fits to the observations. Also, the small optical thickness of the upper layer (about 0.2-0.3) does not seem to require contradiction of the Gehrels, Herman, and Owen hypothesis that predominance of Rayleigh scattering accounts for the wavelength dependence of polarization observed in the Jovian polar regions.

Table 9. Two-Layer, Isotropic-Scattering Models That Best Fit the 8880 Å Observations of the North Polar Region.

	Linear CH$_4$ absorption				Saturated CH$_4$ absorption			
	τ_A	τ_L	τ_B	$\sigma \times 10^2$	τ_A	τ_L	τ_B	$\sigma \times 10^2$
0.9873	0.256	0.19	0.98	0.405	0.548	0.31	0.79	0.330
0.95	0.247	0.19	0.87	0.391	0.526	0.29	0.66	0.327
0.90	0.238	0.19	0.78	0.376	0.500	0.27	0.54	0.320
0.85	0.228	0.20	0.69	0.363	0.468	0.24	0.45	0.313
0.80	0.217	0.20	0.62	0.353	0.430	0.20	0.38	0.306
0.75	0.205	0.20	0.54	0.344	0.390	0.16	0.32	0.298
0.70	0.192	0.20	0.48	0.336	0.352	0.12	0.28	0.301
0.60	0.170	0.20	0.34	0.335	0.325	0.04	0.17	0.350
0.5490	--	--	--	--	0.392	0	0	0.507
0.50	0.156	0.22	0.20	0.471	--	--	--	--
0.3887	0.156	∞	0	0.783	--	--	--	--

70
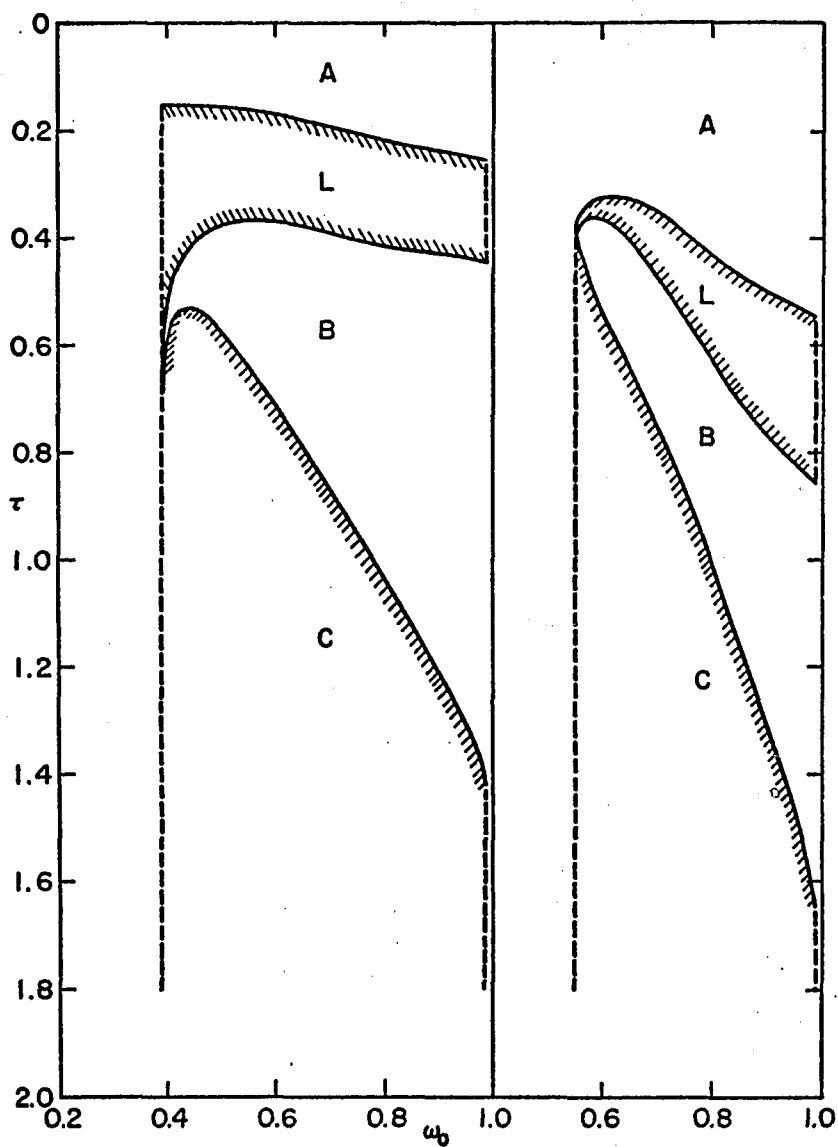
Fig. 15. Layer Thicknesses and Boundary Depths vs ω_0 for the Isotropic-Scattering Models of the North Polar Region.

Curves for the models assuming saturated CH_4 absorption are on the right, those for linear CH_4 absorption on the left.

It is interesting to make a general comparison of the vertical structures of the South Tropical Zone and North Polar Region as revealed by the models. On account of the small τ_L of the North Polar Region, models with $\omega_0 = \omega_0^*$ are the most realistic (for reasons previously discussed), so we shall restrict ourselves to models of this kind. These models are also the ones of greatest interest if one assumes that the Jovian clouds, like terrestrial cumulus and stratus clouds, have scattering mean free paths of only 10 to 100 m. If linear CH_4 absorption is assumed, then τ_A and τ_B are approximately the same in the two regions and correspond roughly to 10 and 35 m-amagats of methane, respectively (assuming $\kappa \simeq 0.4$ cm^2/gm). The striking difference is the thinness of the upper cloud layer in the North Polar Region; it is about one fourth as thick as in the South Tropical Zone. If saturated CH_4 absorption is assumed, τ_A is again about the same for the two regions, but larger by nearly a factor of 2 than in the linear absorption case, corresponding to about 20 m-amagats. τ_B seems to be about two thirds as large in the North Polar Region (approximately 30 m-amagats versus about 45 m-amagats for the South Tropical Zone), and τ_L is only about one fifth as large.

Because of the numerous uncertainties, and particularly because of the noise level of the North Polar observations, these comparisons should be taken to indicate the general structural differences, rather than as well established specifics. However, the conclusion that the upper cloud layer *is* present in the region of latitude +50° but contains only a small fraction of the particles present in the layers of the equatorial zones seems unavoidable.

The procedure followed in fitting the 8880 Å observations of the Red Spot necessarily differs from that used for the South Tropical Zone and North Polar Region because the "limb-darkening curve" of the Spot was obtained in the form of 13 values of the brightness ratio $R(L) = I(L)_{Spot}/I(L)_{Zone}$ corresponding to observation times during the Spot's transit from limb to terminator. In this case, the models are used to compute R values at the same longitudes as the observed values; then the residuals $(R_{obs} - R_{calc})$ are used to calculate the standard deviation, σ_R, which is used to select the best fit from among models of a series in the final step. This procedure requires 13 values of $I(L)_{Zone}$ derived either by interpolation in the South Tropical Zone observations themselves or by computation from one of the models that closely fit the observations. We have used computed values because they are more conveniently obtained and because the significance of the model parameters derived for the Spot is more apparent when they are considered in comparison with those of an appropriate model of the Zone.

Rather than dealing with the five free parameters associated with a general two-layer model of the Red Spot, we have restricted our models to the three simplified types shown in Fig. 16, believing that they represent adequately the range of possible structures. Type I assumes that the clouds of the Spot are uniformly distributed over a great depth, and types II and III assume that the observable differences between Spot and Zone arise from structural differences confined to the lower and upper cloud layers, respectively. These are idealized extremes postulated with the hope that the observations would point out one type as having greater similarity to reality than the other two.

I(a)

$\tau = 0$

τ_{AS}

τ_A

ω_{OS}

ω_0

∞

∞

I(b)

τ_{AS}

τ_A

ω_{OS}

ω_0 τ_L

τ_B

∞

ω_0

∞

II

$\tau = 0$

τ_A

ω_0 τ_L

τ_{BS}

τ_B

ω_{OS}

ω_0

∞

∞

III

τ_{AS}

τ_A

τ_{LS} ω_{OS}

ω_0 τ_L

τ_B

ω_0

∞
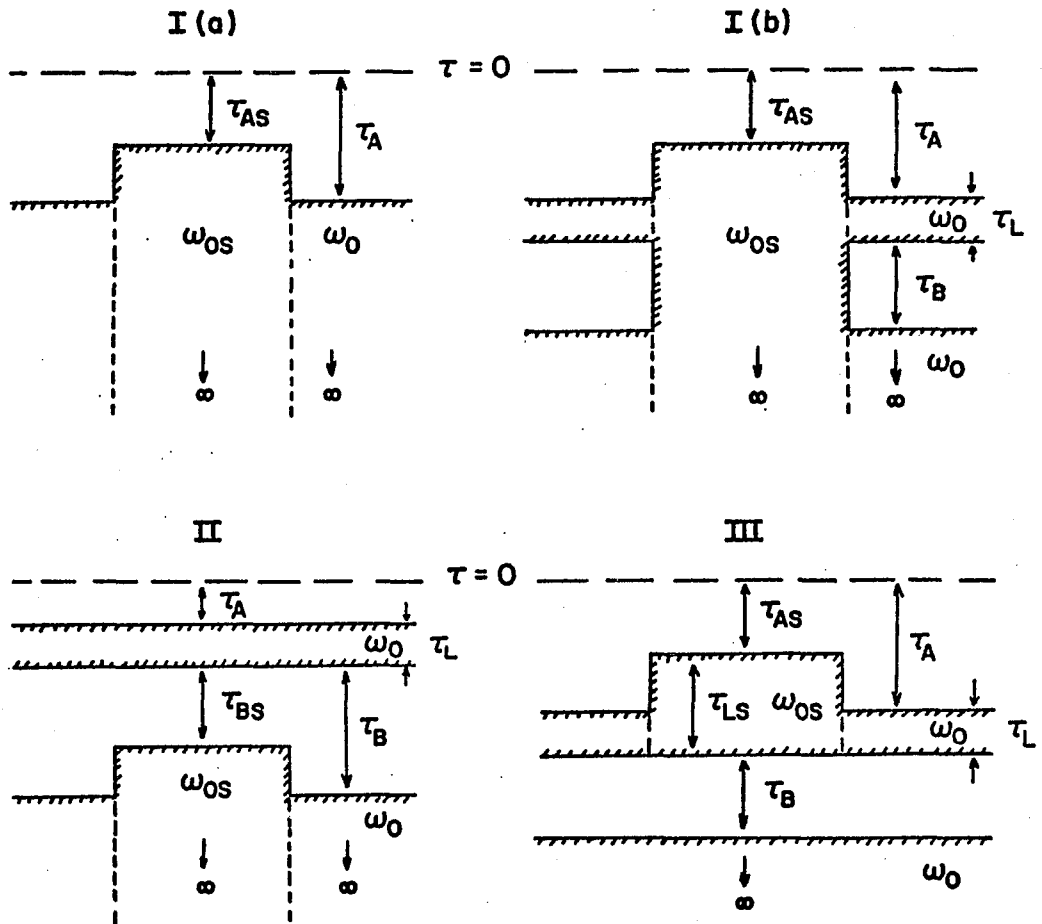
Fig. 16. Schematic Structures of the Three Types of Red Spot
Model.

Type I consists of a semi-infinite Spot emergent from
(a) a semi-infinite and (b) a two-layer cloud model of
the surrounding South Tropical Zone. Type II consists
of a submerged semi-infinite Spot, and Type III consists
of a Spot of finite depth confined to the upper cloud
level of the general two-level cloud structure.

Since models of type I have only two free parameters, a single best-fit model exists. This model is given in Table 10 for linear CH_4 absorption, together with approximate limits arising from observational uncertainty ($\overline{\sigma_{R0}} \simeq 5.0 \times 10^{-2}$). The derived ω_{0S} is low, requiring a scattering mean free path longer than 7 km. Thus the clouds of the Spot are thin haze if the model type is valid. This makes some sense in the context of a situation like that shown in I(a) of Fig. 16, where the semi-infinite clouds of the Zone must also have long mean free paths, but it is much less realistic in the context of the I(b) situation, where the two-layer cloud structure is assumed for the Zone. In the latter case the Spot must be supposed to consist of thin haze while the Zone clouds are required to be much more compact, much more like common terrestrial clouds. This sort of disparity is improbable if one presumes that the processes of cloud formation are basically the same from region to region. Likewise, one expects that the same forces that cause the Zone clouds to form in two discrete layers will also operate in the Spot unless the chemical compositions of the condensates are greatly different in the two regions.

Table 10. Isotropic-Scattering Red Spot Models of Type I (Giving Best Fitting and Approximate Limiting Cases Found).

ω_{0S}	τ_{AS}	$\sigma_R \times 10^2$	Remarks
0.760	0.075	8.30	R increases too rapidly toward limb and terminator
0.778	0.104	5.40	Best over-all fit to the measured R values
0.800	0.140	8.31	R increases too slowly toward limb and terminator

Type II models are dubious from the outset on account of the observations that indicate that the brightness contrast between Spot and Zone remains high even when the Spot is near rise or set ($L \simeq \pm 60°$). The model, on the other hand, requires that the contrast rapidly decrease toward limb or terminator as the Spot is viewed through greater slant thicknesses of upper cloud. As expected, computed contrast ratio curves are convex upward in shape and completely irreconcilable with the observations, even when the optical thickness of the upper cloud is made as small as 0.1. Only when τ_L is made *very* small (less than 0.05) do we obtain satisfactory fits to the observations with type II models. Since these latter models approach the situation of I(a) models, their contrast ratio curves are virtually identical to that of the best-fit model of type I(a) except that, when the limb or terminator is approached, R drops sharply toward unity. These models would be of little interest except for the proposal by Axel (1972) that absorbing dust is thinly distributed throughout the upper atmosphere of Jupiter. Our results with type II models seem to require that this dust layer be optically thin at 0.9 μm wavelength at least. We have also shown that, if such a dust layer is present, then it can safely be ignored in model fitting because its effects are negligible except very near the limbs, regions that we have excluded from consideration.

In fitting type III models to the observations we choose one of the two-layer models fitting the South Tropical Zone observations to serve as the basis for Spot model calculations by (1) providing the $I(L)_{Zone}$ values needed to compute $R(L)$, and (2) fixing two of the five Spot parameters, τ_B and ω_0 for the lower cloud. Three free parameters

remain: τ_{AS}, τ_{LS}, and ω_{0S}. The last is treated as the independent variable; for each selected ω_{0S} a number of models having different τ_{LS} values are computed with τ_{AS} values adjusted so that every model is constrained to have $R(L = 0°) = 1.55$, the approximate contrast ratio observed when the Spot crossed the central meridian of Jupiter's apparent disk. The best over-all fit is selected from among these models on the basis of minimum σ_R.

Limited investigation with type III models (Table 11) indicates that there are many models of this kind (with either type of CH_4 absorption) that are capable of fitting the Red Spot observations. The base models of Table 11 are quite typical of models having ω_0 near to ω_0^* that fit the Zone observations, so choice of any other model of this class to serve as base would not lead to significantly different parameters for the Spot, nor would it much affect the quality of the fits found. The results show that the three free parameters may be changed together in a compensatory way to yield a series of models that all fit in about the same degree. That is, increasing ω_{0S} forces τ_{AS} to increase and τ_{LS} to decrease in order to keep the model reflectivity nearly constant at all longitudes.

For the purpose of making comparisons in Table 11, let us assume that scattering mean free paths are about the same in Spot and Zone clouds and consider the models having $\omega_0 = \omega_{0S} = 0.95$. If linear CH_4 absorption is assumed, the upper cloud layer of the Spot is nearly 50% thicker than that of the Zone, and reaches roughly 3 km higher altitude (on the basis of the approximate absorption coefficient previously discussed). If, on the other hand, saturated absorption is assumed, the

upper cloud is only about 10% thicker in the Spot, but it extends nearly
6 km higher. This seeming paradox is explained by the nearly twofold
greater thicknesses of Spot and Zone upper layers in the saturated case.
In the linear case, where the optical depth is near unity, the thicken-
ing of the upper cloud in the Spot increases its reflectivity in nearly
direct proportion, and this in itself is an important cause of the Spot's
being brighter than the Zone. In the saturated case the upper clouds
are already so thick that the further thickening in the Spot only
slightly increases its reflectivity. Here the smaller depth of absorb-
ing methane over the Spot is *the* major factor accounting for its rela-
tive brightness; the thicker Spot cloud is of importance because it
causes the cloudtops to occur at greater altitude, not because it makes
the clouds more reflective.

Table 11. Isotropic-Scattering Red Spot Models of Type III (Giving Best
Fits Based on Assumed Models of the South Tropical Zone*).

ω_{0S}	Linear CH_4 absorption				Saturated CH_4 absorption			
	τ_{AS}	$\Delta\tau_A$**	τ_{LS}	$\sigma_R \times 10^2$	τ_{AS}	$\Delta\tau_A$**	τ_{LS}	$\sigma_R \times 10^2$
0.93	0.180	0.099	1.14	5.09	0.295	0.205	1.92	5.32
0.95	0.188	0.091	1.07	5.08	0.312	0.188	1.80	5.26
0.97	0.194	0.085	1.00	5.08	0.330	0.170	1.69	5.22
0.99	0.201	0.078	0.95	5.08	0.346	0.154	1.60	5.18

*South Tropical Zone models to which Red Spot models are referred:

	ω_0	τ_A	τ_L	τ_B	$\sigma \times 10^2$
Linear absorption	0.95	0.279	0.70	0.79	0.93
Saturated absorption	0.95	0.500	1.63	2.0	0.57

**$\Delta\tau_A = \tau_A - \tau_{AS}$

In summary, type I models can be fitted to the observations but they are doubtful on physical grounds; type II models are ruled out; and models of type III fit the observations without requiring that the clouds differ much from common terrestrial types with respect to scattering mean free path at least. Although the type III model does an excellent job of accounting for the observed behavior of the Red Spot, it is still possible that the real structure is more complicated. For instance, it is entirely possible that the lower cloud also differs in Spot and Zone, but because the reflective properties of the whole structure are insensitive to changes in structural details occurring at the larger optical depths, this situation cannot be distinguished from that of type III on the basis of our observations. In any case, it is clear that the observed behavior of the Red Spot must be primarily the result of thickening of the *upper* cloud layer, which causes the cloudtops to reach a few kilometers higher than in the adjacent South Tropical Zone.

MODELS WITH FORWARD SCATTERING

Using the cumulus/stratus scattering phase function previously
described, the Jupiter observations have been fitted with models of the
same types as in the case of isotropic scattering. The same methods and
considerations apply to these forward-scattering models, and the reader
is referred to the section on isotropic models for details. Results of
fitting the 9215 Å observations are summarized in Table 12; results of
fitting the 8880 Å observations with two-cloud-layer models are shown in
Tables 13 through 16. Figure 17 illustrates the structures of the South
Tropical Zone models of Table 16. The principal objective of this chap-
ter will be to compare and contrast these results with the corresponding
isotropic models in order to test the accuracy of the van de
Hulst-Grossman scaling relations and to determine the effects on the
various model parameters of assuming two radically different scattering
phase functions.

Tests of van de Hulst-Grossman Scaling

The transformations of van de Hulst and Grossman (1968), namely

$$\tau' = \tau/(1 - g) \tag{38}$$

and

$$1 - \omega_0' = (1 - \omega_0)(1 - g), \tag{39}$$

allow one to take the parameters τ and ω_0 that characterize an isotropic
scattering layer and scale them to yield τ' and ω_0', the parameters of

Table 12. Forward-Scattering Models Fitted to the 9215 $\mathring{A}$ Observations (Giving Best Fits and Approximate Limiting Cases Found).

Region	ω_0	τ_A	$\sigma \times 10^2$	Remarks
South Tropical Zone	0.9956	0.0163	0.93	Model is too bright near the limb
	0.99562	0.0168	0.92	Exact fit at longitudes -45 , 0 , and +45
	0.9958	0.0215	0.86	Best over-all fit to the observations
	0.9960	0.0266	1.10	Model too faint at longitudes greater than 50
North Polar Regions	0.9900	0.085	1.69	Model is too bright near longitudes -45 and +45
	0.9925	0.103	0.36	Best over-all fit to the observations
	0.9945	0.119	1.68	Model is too faint near longitudes -45 and +45
Red Spot	0.9967	0	--	Approximately the best fit to the observations

Table 13. Two-Layer, Forward-Scattering Models That Best Fit the 8880 $\mathring{A}$ Observations of the South Tropical Zone.

ω_0	Linear absorption				Saturated absorption			
	τ_A	τ_L	τ_B	$\sigma \times 10^2$	τ_A	τ_L	τ_B	$\sigma \times 10^2$
0.9958	0.324	2.58	0.80	1.50[a]	0.550	4.73	0.55	0.82
0.982	0.310	2.55	0.56	1.26[a]	0.516	5.8	0.36	0.67
0.968	0.288	2.50	0.41	1.12	0.474	7.	0.2	0.68
0.954	0.271	2.45	0.29	1.00	0.435	∞	0	1.04
0.926	0.238	1.80	0.09	0.81	--	--	--	--
0.9103	0.234	0	0	0.69	--	--	--	--

[a]Marginal fits.

Table 14. Two-Layer, Forward-Scattering Models That Best Fit the 8880 Å Observations of the North Polar Region (Near-Continuum Values of ω_0 Only).

ω_0	Linear absorption				Saturated absorption			
	τ_A	τ_L	τ_B	$\sigma \times 10^2$	τ_A	τ_L	τ_B	$\sigma \times 10^2$
0.9958	0.269	0.500	0.927	0.384	0.564	0.81	0.74	0.313
0.982	0.254	0.475	0.796	0.353	0.527	0.64	0.58	0.294

Table 15. Forward-Scattering Red Spot Models of Type I (Giving Best Fit Values of τ_{AS} and ω_{0S}).

	ω_{0S}	τ_{AS}	$\sigma_R \times 10^2$
Linear CH$_4$ absorption	0.940	0.144	5.42
Saturated CH absorption	0.960	0.258	5.27

Table 16. Forward-Scattering Red Spot Models of Type III (Giving Best Fit Models Based on Assumed Models of the South Tropical Zone*).

ω_{0S}	Linear CH$_4$ absorption				Saturated CH$_4$ absorption			
	τ_{AS}	$\Delta\tau_A$	τ_{LS}	$\sigma_R \times 10^2$	τ_{AS}	$\Delta\tau_A$	τ_{LS}	$\sigma_R \times 10^2$
0.9958	0.244	0.081	4.64	5.64	0.371	0.179	5.68	5.15

*South Tropical Zone models to which Red Spot models are referred:

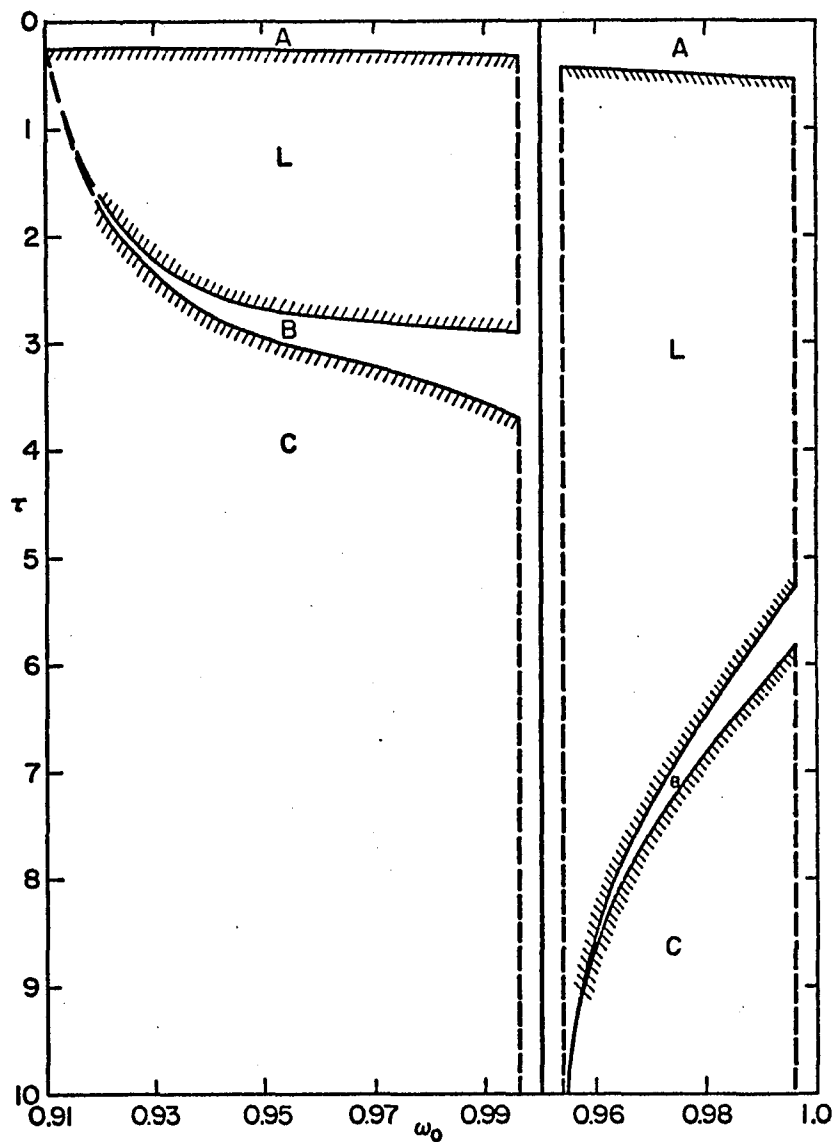|	ω_0	τ_A	τ_L	τ_B	$\sigma \times 10^2$
Linear absorption	0.9958	0.324	2.58	0.799	1.50
Saturated absorption	0.9958	0.550	4.73	0.547	0.818

Fig. 17. Layer Thicknesses and Boundary Depths vs ω_0 for the
Forward-Scattering Models of the South Tropical Zone.

Curves for the models assuming saturated CH_4 absorption
are on the right, those for linear CH_4 absorption are
on the left.

an anisotropic scattering layer having *approximately* the same reflection and transmission properties. The quantity g is the asymmetry parameter of the anisotropic phase function and has values between 0 and 1, depending on how strongly forward-scattering the phase function is ($g = 0.850$ for the cumulus/stratus phase function we have used).

Our parallel series of isotropic and forward-scattering models provide opportunities to test both van de Hulst-Grossman equations by comparing τ' and ω_0' values derived from model fitting with corresponding values derived from scaling isotropic model results. The most clear-cut case is that of the model fits to the 9215 $\overset{\circ}{A}$ observations (Table 12). Here, both isotropic and cumulus/stratus assumptions yield models that fit equally well. Also, when uncertainties are taken into account, the derived values of τ_A (about 0.01 for the Zone, 0.1 for the North Polar Region, and 0 for the Spot) are nearly the same for both phase functions. As expected on the basis of Eq. (39), the ω_0 values characterizing the semi-infinite cloud decks *are* different in corresponding isotropic and cumulus/stratus models, being nearer unity in the latter case. However, if one uses ω_0 values derived from fitting isotropic models and Eq. (39) to predict corresponding cumulus/stratus model ω_0' values, one finds that these predicted values are consistently nearer unity than the ω_0' values derived from actually fitting cumulus/stratus models to the observations. Comparisons of predicted and model-derived ω_0' values are summarized in Table 17. The last column of this table indicates that all three Jupiter regions considered have model-derived cloud particles that are 2 to 4 times as likely to absorb an incident photon as are the corresponding scaling-predicted cloud particles.

84

Table 17. Comparison of Continuum ω_0 Predicted from Isotropic Models with That Derived from Model Fittings.

Region	Isotropic $1-\omega_0$	Predicted $1-\omega_0'$	Derived $1-\omega_0'$	$\dfrac{(1-\omega_0')_D}{(1-\omega_0')_P}$
South Tropical Zone	0.012 ± 0.001[a]	0.0018 ± 0.0002	0.0042 ± 0.0002	2.3
North Polar Region	0.013 ± 0.006	0.0020 ± 0.0009	0.0075 ± 0.0025	3.8
Red Spot	0.007	0.001	0.003	3
				(ave. = 3.03)

[a]Approximate range allowed by observational uncertainties.

This apparent failure of the van de Hulst-Grossman scaling relation almost certainly arises out of two particulars of the case we are considering, namely: (1) The cumulus/stratus phase function has a pronounced backscattering lobe or "glory peak," and (2) our Jupiter observations were obtained when the phase angle of the planet was only 2.7°. A layer composed of such backscattering particles shows marked increase in reflectivity as the phase angle decreases from about 10° to 0° because of the increased contribution of single and low-order multiple scattering arising from the glory feature of the phase function. Similar layers of particles having smooth, featureless phase functions like the isotropic or Henyey-Greenstein functions show no such enhanced reflectivity at small phase angles. (Figure 4 of Hansen, 1969b, provides a striking example of these effects for the cases of terrestrial cloud and of Henyey-Greenstein phase functions.) The van de Hulst-Grossman relation fails to predict ω_0' correctly because it does not take the localized glory enhancement into account. The shape of the phase function enters in only through the asymmetry parameter, that is, as an integral containing only gross information about the function's shape which is insensitive to the presence or absence of relatively small features like the glory or rainbow peaks. In the model fitting, the glory enhancement *is* taken into account; the increased low-order scattering contribution is compensated for by making the particles more absorbing, yielding a cloud surface whose reflectivity matches the observations.

Another failure of van de Hulst-Grossman scaling is observed in the case of the two-layer model fits to the 8880 Å observations. Here one applies Eq. (38) to the upper cloud layer optical depths, τ_L, derived

from isotropic model fitting in order to predict the corresponding τ_L'

values, which in the case of the cumulus/stratus phase function should

be 6.7 times larger. However, τ_L' values derived from model fitting are

consistently only about 3 times larger than their isotropic counterparts.

This case is less clear-cut than that of the 9215 Å models because other

variables besides τ_L (τ_A, τ_B, ω_0, etc.) can enter into the comparison of

predicted and derived values. In Table 18 we have selected for compari-

son models having continuum ω_0 and ω_0' values and have segretated the

models according to Jupiter region and type of CH_4 absorption assumed so

as to keep the influence of the other variables to a minimum. The last

column of this table indicates that the van de Hulst-Grossman predictions

are about twice as large as the τ_L' values derived from cumulus/stratus

models, with no definite dependence on region or type of absorption

evident.

Table 18. Comparison of Upper Cloud Layer τ_L Predicted from Isotropic Models with That Derived from Model Fittings.

Region	Type of CH_4 absorption	Isotropic τ_L	Predicted τ_L'	Derived τ_L'	$\dfrac{(\tau_L')_P}{(\tau_L')_D}$
South Tropical Zone	Linear	0.7	4.7	2.6	1.8
	Saturated	1.4	9.3	4.7	2.0
North Polar Region	Linear	0.2	1.3	0.5	2.6
	Saturated	0.3	2.0	0.8	2.5
Red Spot	Linear	1.0	6.7	4.6	1.5
	Saturated	1.6	11	5.7	1.9

This second failure of scaling is of the same sense and of about
the same magnitude as that observed in the case of the 9215 Å models.
In this case, if the upper cloud layer of the model were to be made as
thick as scaling requires, it would be too strongly reflecting to be
consistent with observation because the enhancement due to the glory fea-
ture has not been taken into account in the asymmetry parameter of Eq.
(38). In model fitting, however, the glory enhancement is automatically
compensated for by making the upper cloud layer thinner (hence less re-
flective) than it would have to be if there were no glory.

From these cases we conclude that van de Hulst-Grossman scaling
of isotropic parameters must be used with caution in the case of Jupiter
and the outer planets since they are observed at small phase angles and
since most of the realistic scattering phase functions we might consider
contain the glory feature or a back-scattering peak of some other origin.
Scaling yields consistent results, but predicted $(1 - \omega_0')$ may be too small
and predicted τ_L' too large by several times unless some sort of "effec-
tive asymmetry parameter" is devised that takes the back-scattering en-
hancement into account.

Effects of Changing the Phase Function

Comparison of the cumulus/stratus models (Tables 13 through 16)
with their isotropic counterparts (Tables 7 and 9 through 11), with par-
ticular emphasis on models having near-continuum ω_0 (or ω_0', as the case
may be), leads to the following generalizations:

1. The best-fitting models for each region and type of CH_4
absorption fit the observations about equally well regardless of which

phase function is assumed. The only exception found is that of the cumulus/stratus models of the South Tropical Zone (Table 13), where linear absorption is assumed. These models yield significantly poorer fits than the corresponding isotropic models--so poor in fact that it is questionable whether they can be considered fits to the observations at all. This case probably arises in part from the general tendency of models with saturated CH_4 absorption to yield better fits (smaller σ) than those with linear absorption, all else being equal.

2. As already mentioned, the upper cloud layer optical thickness is about three times greater in the forward-scattering models than in the isotropic ones. In the six cases where comparison was made (three regions with either linear or saturated absorption), the factors range from 2.5 to 4.5 and the mean is 3.4. The saturated and linear South Tropical Zone models, based on the most precise observations, yield factors of 3.4 and 3.6, respectively.

3. The optical depths of the A and B methane layers are essentially unchanged by the change of phase function. This is what we expect, for if we had an isotropic layer in a model fitting the observations and if we could find a forward-scattering layer with *exactly* the same reflection and transmission properties, we could substitute the one for the other without any other changes in the model and still obtain exactly the same quality of fit. In practice, the reflection and transmission properties can only be made approximately the same, requiring some adjustment of τ_A and τ_B to compensate for the differences and make the model fit the observations as closely as possible. Even so, the constancy of the CH_4 optical depths holds to a surprising degree. For

instance, in comparing τ_A values of isotropic and cumulus/stratus models
of the same region and absorption type, we find only one case of six
where the difference is greater than 10%. Agreement of corresponding τ_B
values is just as good in the case of the North Polar Region models
(0.98 versus 0.93 and 0.79 versus 0.74), but poorer in the case of the
South Tropical Zone models (1.03 versus 0.80 and 1.25 versus 0.55),
probably because the upper cloud layer is 4 to 5 times thicker in the
Zone than in the North Polar Region. The greater the optical depth of
the overlying layers, the more uncertain τ_B becomes; when the B layer of
methane is largely obscured from view by the clouds above it, it is pos-
sible to make relatively large changes in τ_B without significantly
changing the reflectivity of the model as a whole. Also, since τ_B is
the least firmly fixed parameter in this situation, it is the most likely
to change in response to changes in reflection and transmission that oc-
cur when "equivalent" forward-scattering cloud layers are interchanged
with isotropic ones. As evidence that such changes in τ_B (and to a
lesser extent τ_A) *do* occur, we note that τ_B is *always* smaller and τ_A is
always larger for the cumulus/stratus model than for the corresponding
isotropic model, and further, that the difference between corresponding
τ_B values is largest when τ_L and $\tau_L{}'$ are largest. Hence, our opening
statement that τ_A and τ_B are essentially the same for both phase func-
tions holds as a useful first-order approximation, but is subject to
considerable error when the upper cloud layer is optically thick.

Effects of the Degree of Methane Band Saturation

The models fitted to the observations have incorporated one or the other of two simplified extreme assumptions regarding the strength of the 8880 Å band: (1) It is a weak band, i.e., it is formed on the linear part of the curve of growth, or (2) it is a strong (saturated) band, effectively formed entirely on the square-root part of the curve of growth. Two parallel series of models for each region and phase function result, differing only in the type of methane absorption assumed. We shall use these to determine the effects of different degrees of saturation on the other model parameters derived.

There is a general tendency for models assuming saturated absorption to yield somewhat better-quality fits to the observations. For the Red Spot and the North Polar Region the quality is so nearly the same that the differences between linear and saturated fits cannot be considered significant. The better quality of the South Tropical Zone observations allows more discrimination, however. Here we find that the saturated models are clearly better than their linear counterparts. For example, the near-continuum ω_0 cumulus/stratus models assuming saturated absorption are rather good fits, but the corresponding linear models are only marginal-quality fits.

The change from linear to saturated absorption leads to changes in all three optical depth parameters, but these changes occur in a consistent pattern that seems to be independent of region or phase function. The upper cloud layer is roughly 1.7 times thicker in the saturated models than in the corresponding linear models (the factor 1.7 is the average of six cases where the range is 1.2 to 2.0). The optical depths

of the A and B methane layers are, respectively, 1.8 and roughly 0.8

times greater in the case of saturated absorption. The increase factor

for the A layer seems to show some dependence on upper cloud thickness,

being 2.1 for the North Polar Region and about 1.7 for the Spot and Zone,

but this is quite uncertain. The increase factor for the B layer rests

mainly on values for the N.P.R., where the upper cloud layer is thin

enough that model-derived τ_B values are entirely reliable.

Effects of Reducing the Single-Scattering
Albedo of the Cloud Layers

In the case of the cumulus/stratus models, as in the case of the

isotropic models discussed previously, we have investigated the effects

of having the cloud particles increasingly sparsely distributed in a

methane matrix by means of decreasing the independent parameter ω_0 from

its upper limit, the continuum value ω_0^*. Models of the South Tropical

Zone (Table 13) cover the entire permitted range from ω_0^* to the lower

limit ω_0, where the two cloud layers merge into a single, semi-infinite

cloud deck (the limiting value of ω_0 being derived, in fact, by fitting

a simple model consisting of a semi-infinite cloud and an overlying

methane layer to the 8880 Å observations). We find that, in contrast to

the corresponding isotropic models, the lower-limit ω_0 values *do not* re-

quire that the clouds be extremely thin haze; even for $\omega_0 = 0.91$ the

scattering mean free path is still less than 3 km.

It is useful to examine the model series of the South Tropical

Zone and North Polar Region in order to determine general trends in the

behavior of τ_A, τ_L, and τ_B with decreasing ω_0. Qualitative behavior,

according to region, type of methane absorption, and phase function is

summarized in Table 19. Here little weight is given to the behavior of
models having ω_0 near the lower limit, since (as previously shown in the
discussion of the isotropic models) values of τ_B and τ_L cannot be fixed
accurately in this case; τ_B and τ_L can be increased or decreased over a
wide range without much reduction in the quality of the fit to the ob-
servations (provided that *both* are increased or decreased at the same
time). Table 19 shows that, regardless of region, phase function, or
type of absorption, the optical depths of both methane layers decrease
as ω_0 decreases. Since an increasing fraction of the total absorption
occurs *within* the cloud layers, this trend is not surprising. It *is* in-
teresting that, although τ_B decreases rapidly, τ_A decreases by only 20%
to 40% over the whole range of ω_0. Evidently, the presence of an upper
methane layer is firmly required by the observations, and further, its
thickness is constrained within quite narrow limits and is largely un-
affected by the variations of other parameters and assumptions.

The behavior of τ_L with decreasing ω_0 is much less clear-cut.
Table 19 reveals no definite patterns of similarity with either region
or phase function, but there does seem to be a tendency for τ_L to in-
crease or decrease slowly when linear CH_4 absorption is assumed, but to
increase or decrease rapidly when saturated absorption is assumed. A
similar pattern is also seen in the decrease of τ_A with decreasing ω_0;
the rate of decrease is 2 to 4 times greater for saturated absorption
than for linear. These trends are reflected in the tendency for satu-
rated model series to terminate at higher ω_0 values than their linear
counterparts, the more rapid rates of change in the saturated series
causing them to extend over only about half the range of ω_0.

Table 19. Qualitative Behavior of the Two-Layer Model Parameters as ω_0 Is Decreased below ω_0^*.

Type of CH_4 absorption	Region	Phase function	τ_A	τ_L	τ_B
Linear	S.Tr.Z.	Iso.	decreases very slowly	increases slowly	decreases rapidly
		C/S	"	decreases slowly	"
	N.P.R.	Iso.	"	constant	"
		C/S	"	decreases slowly	"
Saturated	S.Tr.Z.	Iso.	"	increases rapidly	?[a]
		C/S	"	increases rapidly	decreases rapidly
	N.P.R.	Iso.	"	decreases moderately	"
		C/S	"	decreases rapidly	"

[a] τ_B values for models having $\omega_0 < \omega_0^*$ are quite uncertain here because τ_L is large and increasing rapidly as ω_0 decreases.

CONCLUSIONS

The properties of the most interesting of the models that repro-
duce the 8880 Å limb-darkening observations are summarized in Tables 20
and 21. In these models the single-scattering albedo is constrained to
be the same for both cloud layers and equal to the continuum albedo
found from the 9215 Å observations, hence it is implicitly assumed that
scattering mean free path is similar to that of terrestrial clouds (tens
or hundreds of meters). These models are also interesting because they
involve the fewest free parameters; once the scattering phase function
and linear or saturated CH_4 absorption are chosen, only the three opti-
cal depths τ_A, τ_B, and τ_L can be adjusted to make the model fit the
observations.

The values found for the three parameters depend markedly upon
the types of particle scattering and gas absorption assumed, but given a
particular set of assumptions it is found that only certain limited
ranges of the optical depth parameters are allowed. In the case of the
South Tropical Zone (where the most precise observations were obtained)
it is possible to assign approximate ranges to each parameter that indi-
cate the limits permitted by observational uncertainty (see Table 20).
Not surprisingly, parameter uncertainty increases in proportion to the
depth within the atmosphere of the associated layer, being least for the
uppermost A layer and greatest for the lower (B) methane layer, particu-
larly when the latter is largely obscured by a thick upper cloud layer
(L).

Table 20. Two-Layer Cloud Model for the South Tropical Zone.

Cloud-layer parameters:

Phase function	ω_0	τ_L(lin.)	τ_L(sat.)
Isotropic	0.988 ± 0.002	0.7 ± 0.05	1.4 (1.0 - 1.5)
Cumulus/stratus	0.9958 ± 0.0002	2.6 ± 0.1	5 ± 1
Henyey-Greenstein[a]	0.9982 ± 0.0003	4.7 ± 0.3	9.3 (6.7 - 10.0)

Methane-layer parameters:

τ_A(lin.)	τ_A(sat.)	τ_B(lin.)	τ_B(sat.)
0.31 ± 0.03	0.54 ± 0.05	0.9 ± 0.2	∿1 (>0.5)

[a]Computed from isotropic values by van de Hulst-Grossman scaling with g = 0.850; results apply to any phase function having this g but no features near 180° scattering angle.

Table 21. Two-Layer Cloud Models for the North Polar Region and Red Spot.

Cloud-layer parameters[a]:

Phase function	North Polar Region		Red Spot	
	τ_L(lin.)	τ_L(sat.)	τ_L(lin.)	τ_L(sat.)
Isotropic	0.19 (0.27)	0.31 (0.22)	1.0 (1.4)	1.6 (1.1)
Cumulus/stratus	0.50 (0.19)	0.81 (0.16)	4.6 (1.8)	5.7 (1.1)

Methane-layer parameters[b]:

Phase function	North Polar Region				Red Spot	
	$\tau_A(L)$	$\tau_A(S)$	$\tau_B(L)$	$\tau_B(S)$	$\tau_A(L)$	$\tau_A(S)$
Isotropic	0.26	0.55	0.98	0.79	0.20	0.34
Cumulus/stratus	0.27	0.56	0.93	0.74	0.24	0.37

[a]Single-scattering albedo is 0.988 (isotropic) or 0.9958 (cumulus/stratus). Only best-fit optical depths are given; numbers in parentheses are the ratios of the North Polar Region or Red Spot optical depths to the corresponding Zone optical depth.

[b]Best-fit values only; the B-layer optical depths for the Red Spot are assumed to be similar to those of corresponding Zone models.

From Tables 20 and 21 it is clear that the greatest source of
uncertainty in the details of vertical structures concerns which scat-
tering phase function and what degree of saturation are appropriate for
Jupiter. Some clarification of these questions is expected to come from
analysis of data obtained during the recent flyby of the Pioneer 10
spacecraft and from laboratory studies of the visible and near infrared
absorption bands of methane, both under way at the present time. Lacking
such information at the outset, we have attempted to find limits and be-
havior patterns for the parameters by considering different extreme
cases. Some of the generalizations drawn from this kind of investiga-
tion are straightforward, but others not yet mentioned in the literature
may find useful applications elsewhere, particularly in cases where scat-
tering models are used to interpret observations of the outer planets.

First, let us consider the effects of changing only the scatter-
ing phase function. We have found that it is possible to replace the
isotropic-scattering layers with forward-scattering layers having approx-
imately the same diffuse reflection and transmission properties without
significantly affecting the quality of the fit to the observations or
the values of the absorption optical depths of the A and B layers. As
expected from the van de Hulst-Grossman equations, making such a change
in phase function requires increases in both single-scattering albedo
and cloud optical depth. However, if we are considering a phase func-
tion with a backscattering lobe ("glory") like the cumulus/stratus
function we·have used, and if we are considering observations made at
small phase angles, then the parameters predicted from isotropic parame-
ters by van de Hulst-Grossman scaling are systematically too large

because the localized increase in reflectivity arising from the sharp
glory feature is not taken into account. The sizes of the discrepancies
between predicted and found values can be appreciated from Table 20,
where we have included parameters derived by scaling using the asymmetry
parameter for the cumulus/stratus phase function. Scaling predicts
cloud optical depths 6.7 times greater and $(1 - \omega_0)$ 6.7 times smaller for
the cumulus/stratus phase function. It is found that these quantities
do indeed scale consistently, but the scale factor is in the range 2 to
3 rather than 6.7. That is, in our case van de Hulst-Grossman scaling
would correctly predict cumulus/stratus parameters if the actual asymme-
try parameter were replaced by an effective value, $g_{eff} \simeq 0.6$.

The question of which phase function is best for the clouds of
Jupiter remains. Isotropic scattering is unrealistic and results ob-
tained are useful only for scaling to other phase functions. As previ-
ously discussed, there is considerable room for doubt in the case of the
cumulus/stratus phase function because we are taking a phase function
derived for terrestrial water-droplet clouds and applying it to the
solid ammonia particles of Jupiter's upper atmosphere. We feel that the
over-all shape and degree of asymmetry of this phase function are suita-
ble, but there is the possibility that the Jovian cloud particles are
irregular crystalline aggregates rather than approximately spherical
shapes. If this is so, then the details of the phase function will be
different. The glory peak, which arises from spherical shape, would be
weakened in proportion to the irregularity of the particles and might be
absent altogether. Supposing that the glory is absent leads us back to
the parameters computed from isotropic results by van de Hulst-Grossman

scaling with $g = 0.850$. Hence this case and the cumulus/stratus case can be considered limiting possibilities for the variation of model parameters with phase function. This still leaves the cloud-layer parameters τ_L and $(1 - \omega_0)$ uncertain by a factor of 2 or more (see Table 20).

Changing the degree of saturation assumed for the absorption band leads to changes in all three optical depth parameters which follow a pattern that seems independent of the phase function or region involved. In going from purely linear to completely saturated (square-root) absorption, there is a nearly twofold increase in τ_A and τ_L and a small decrease in τ_B. Because of these variations it is highly desirable to determine which (if either) regime of the curve of growth is most appropriate for the CH_4 8873 Å band of Jupiter.

Preliminary results from laboratory measurement of the band by Dick (1974) indicate that the region of transition from linear to square root growth is where the Jovian band is formed. At abundances of from 10 to 20 meter-amagats there is already small but significant departure from linear growth, but the region of strictly square-root growth is not reached until abundance grows to about 10^3 m-am or greater. The absorption coefficient is found to be about 0.3 cm^2/gm (or unit optical depth for 45 m-am) at 8880 Å and for abundance on the order of 20 m-am, in good agreement with our previous estimate based on the strength of the Jovian band: 0.4 cm^2/gm, or unit optical depth for 35 m-am.

In light of Dick's findings we see that neither the linear nor the saturated models can be realistic; they only serve the purpose for which they were intended, i.e., to determine the limits of uncertainty in the model parameters arising out of uncertainty as to the importance

of curve-of-growth effects. Reality must lie somewhere between the lin-
ear and saturated extremes, but where? Precise answers will have to
come from future models that incorporate curve-of-growth effects realis-
tically on the basis of the final results of the laboratory studies. At
this point the saturated models seem to have the slight edge. We have
previously mentioned the general tendency of saturated models to yield
closer fits to the observations than their linear counterparts. This
comes about because the linear models have difficulty in reproducing the
observed brightness near the limbs; they consistently show too rapid de-
crease in brightness for longitudes outside about -50° and +50°. The
abundance along an in-and-out path through *only* the A layer of methane
is already 40 to 80 m-am near the limbs ($L = \pm60°$), hence we are off the
linear part of the curve of growth and well into the transition part
even if we ignore the contribution of the B layer.

Because the South Troptical Zone is, of our three regions, prob-
ably the most typical of Jupiter as a whole, we have compared our results
for it with the results of previous work in Table 22. Our results for
τ_L and for w_A and w_B (methane abundances) are given as two values sepa-
rated by a hyphen; the first value is for linear methane absorption, the
second for saturated absorption. If the absorption coefficient is taken
to be 0.3 cm^2/gm, the values of w_A and w_B will be 30% larger than those
given in Table 22. Where possible, we have given best values and ranges
allowed for the results of other work. Allowing for these uncertainties,
the agreement of the various results is generally good. We find a
thinner upper cloud layer ($\tau_L \simeq 1$ for isotropic scattering), but in view
of the considerably greater uncertainty ranges associated with the other

Table 22. Comparison of Our Two-Layer Cloud Models of the South Tropical Zone with Similar Models of Others.

Cloud-layer parameters (isotropic scattering):

Source	ω_0	τ_L	Type of observation
Our work	0.988	0.7-1.4	Limb darkening in CH_4 8873 Å band
Danielson and Tomasko (1969)	0.95-0.98	~2	Whole-disk equivalent widths of H_2 quadrupole 4-0 and 3-0 bands (at about 6400 and 8200 Å)
Axel (1972)	~0.99	~3.5(2-5)	Whole-disk equivalent widths of H_2 4-0 and 3-0 bands and of CH_4 $3\nu_3$ band at about 11,000 Å
Bergstralh (unpublished)	~0.99	~2(1-3.5)	Equivalent widths of R-branch lines of CH_4 $3\nu_3$ band measured at many points on Jupiter's disk

Methane-layer abundances:

Source	w_A	w_B	Remarks
Our work	~10-20 m-am	~30-40 m-am	Assumes 8880 Å κ = 0.4 cm^2/gm
Danielson and Tomasko (1969)	20	47	Predicted from abundance model (their Table 1, 130° model)
Axel (1972)	25	62	Computed from H_2 abundances and CH_4 mixing ratio of his preferred model
Bergstralh (unpublished)	10 ± 2	40 ± 10	Values for his best-fit model with ω_0 = 0.99 and τ_L = 2

methods, this is probably not an important difference. Hunt (1973) has computed theoretical center-to-limb variations for the H_2 quadrupole lines and for the CH_4 $3v_3$ band, which led him to conclude that, for Jupiter considered as a whole, the upper cloud layer must be optically *thin*, considerably thinner in fact than anyone has previously contemplated. From the parameters of his models we derive optical depths of a few tenths for his upper cloud layers. It may be that this is nearer the truth and perhaps a re-evaluation of some of the previous work using newer radiative transfer techniques is called for.

Perhaps more interesting than the specific values of structural parameters are the structures of the Red Spot and North Polar Region relative to that of the South Tropical Zone. Regardless of which phase function or degree of saturation is considered, the same pattern of similarities and differences emerges from the results of Tables 20 and 21. The North Polar Region is *not* free of high-level clouds as Gehrels, Herman, and Owen (1969) have supposed, but the upper cloud layer is optically thin, having only about 1/5 the thickness found in the Zone. The cloud layers occur at about the same levels in the atmosphere; the thicknesses of the A and B layers of methane are nearly the same in both the Zone and the N.P.R. The Red Spot is a region where the upper cloud layer is optically thicker and extends to 5 ± 3 km greater altitude. Both of these structural differences cause the Spot to appear bright relative to the Zone at 8900 $\overset{\circ}{A}$, but the latter is the more important factor. The Spot is brighter mainly because of the smaller abundance of methane above it, but also because the thicker cloud reflects more of the light before it can be absorbed by the lower methane layer.

The meteorological causes giving rise to these structural differences are unknown. Kuiper (1972) has come forth with some audacious speculations. He proposes that the Red Spot is the visible manifestation of a large-scale, steady-state thunderstorm composed of "...a highly active area some 3,000 kilometers in diameter beneath a thick cirrus cover (the visible spot) some six times that extent...." This hypothetical structure is breathtakingly similar to the picture of the Spot we have described above. Kuiper's theory of Jupiter's atmospheric circulation considers the South Tropical Zone to be in the latitude where the northeast and southeast trade winds converge to produce storm clouds "with tremendous anvils breaking to form cirrus in the upper troposphere." If this is so, then the upper cloud thickness of the Zone may be atypically large. Perhaps the average cloud thickness is actually more like that found in the North Polar Region.

More observational evidence is clearly required. Analysis of our pole-to-pole 8880 $\text{\AA}$ scans mentioned previously should yield interesting information concerning the structural differences between belts and zones, and about the origin of the polar hoods. (Preliminary indications are that the hood is caused by a very thin, very high layer of scatterers.) Observations in a weak band, CH_4 6190 $\text{\AA}$, are planned for the near future. Scanner observations of Saturn at 8880 and 9215 $\text{\AA}$ have been obtained and will be analyzed as soon as final results of Dick's laboratory work become available.

APPENDIX

GLOSSARY OF FREQUENTLY USED SYMBOLS

A   A label or subscript identifying the uppermost absorbing layer of a model atmosphere (usually the upper methane layer in the two-layer cloud model).

B   A label or subscript identifying the lower methane layer of the two-layer cloud model.

C   A label or subscript identifying the lower cloud layer of the two-layer cloud model.

F Flux density; the radiant power received per unit area and per unit wavelength interval. F is used with various subscripts and superscripts that identify the source of the radiation.

G Diffuse reflectivity of a small region on Jupiter, defined as the ratio of the observed flux density to the flux density from a Lambert surface of unit albedo placed at Jupiter's distance from the sun and oriented perpendicular to the direction of the sun. G is used with subscripts identifying the point (or set of points) referred to, e.g., G_0 stands for the reflectivity at the central-meridian point ($L = 0°$) of a scan line following a specified circle of latitude.

g Asymmetry parameter characterizing the degree of forward scattering of the single-scattering phase function. It is defined as the integral over all solid angles of the phase function weighted by the cosine of the scattering angle divided by 4π. Its value ranges from zero (for isotropic scattering) to just less than unity.

I Specific intensity; the radiant power received per unit area, per unit wavelength interval, and per unit solid angle. I is used with various subscripts and superscripts that identify the source of the radiation (or measured signal in connection with the observations).

k Atmospheric extinction coefficient (magnitudes per air mass).

L Planetocentric longitude measured from $L = 0°$ at the central meridian positive toward the setting edge of the planetary disk.

L A label or subscript identifying the upper cloud layer of the two-layer cloud model.

103

L The number of points used in Gaussian quadratures involved in thin-layer "doubling" to obtain S and T functions for scattering layers. (This usage of L occurs only in one brief section of the text, where the meaning intended is clear from the context.)

l_s Scattering mean free path.

l_a Absorption mean free path.

l Planetocentric latitude, measured positive northward from the equator.

m Order of a term or coefficient of a Fourier series: $m = 0, 1, 2, \ldots$.

M The maximum value of the Fourier order, m.

p The single-scattering phase function that gives the probability that a scattered photon will be diverted from its original path to a new path making a particular angle (the scattering angle) with the original path. Subscripts S and T are often used to differentiate forms applying to reflected and transmitted photons, respectively.

R Ratio of Red Spot brightness to South Tropical Zone brightness, both brightnesses referring to the same longitude.

r_0 Seeing quality parameter for blurring according to a point-spread function of Gaussian form.

S Chandrasekhar's scattering function, which specifies the angular distribution of light diffusely reflected from a layer or from a multilayered scattering atmosphere. S is often used with subscripts specifying particular layers.

T Chandrasekhar's transmission function, which specifies the angular distribution of light diffusely transmitted by a scattering layer.

X Standard intensity profile scan-direction coordinate.

X Effective air mass function for Jupiter's atmosphere at 8880 $\overset{\circ}{A}$.

x Intensity profile scan direction coordinate (nonstandard profiles).

x Terrestrial air mass of object observed (Jupiter).

x,y and x',y' Cartesian coordinate systems locating points in the telescopic image plane (used in connection with "seeing" convolution expressions).

θ Scattering angle, the angle through which a photon is diverted from its original path by scattering. Subscripts S and T are sometimes used to distinguish angles corresponding to reflection and transmission, respectively.

κ Mass absorption coefficient (area per unit mass).

λ Wavelength.

μ The cosine of the zenith angle of the earth as seen from a point on Jupiter's surface.

μ_0 The cosine of the zenith angle of the sun as seen from a point on Jupiter's surface.

ρ Mass density (mass per unit volume).

σ Parameter indicating the quality with which a theoretical limb darkening curve fits its corresponding observational limb darkening curve. It is the standard deviation of the differences between the observational mean and the model G/G_0 values at a number of approximately equally spaced longitudes, 13 of them in the case of the South Tropical Zone and nine in the case of the North Polar Region.

σ_0 Approximate standard deviation characterizing the scatter of observation points about the mean G/G_0 at a particular longitude.

$\overline{\sigma_0}$ The average of σ_0 over all longitudes considered.

σ_R Parameter indicating the quality with which a theoretical Red Spot R curve fits the observed values of R. It is the standard deviation of the differences between model and observed values at the 13 longitudes where reliable values of R were obtained. (σ_R is used for the standard deviation of the R measurements themselves only in Table 4; the average of these standard deviations for all measurements at either wavelength is referred to as $\overline{\sigma_{R_0}}$.)

τ Optical depth (scattering, absorption, or total, according to the context) at either 8880 or 9215 Å. Various subscripts are used to identify layers and to distinguish Spot layers from Zone layers. The superscript ' indicates scaled (forward-scattering) optical depth.

$\phi - \phi_0$ The difference between the azimuth angles of the earth and sun as seen from a point on Jupiter's surface. The zero point and direction of measurement of individual azimuth angles is arbitrary as long as the convention is the same for both ϕ and ϕ_0. The value of $\phi - \phi_0$ is always less than or equal to 180°.

ω_0 Single-scattering albedo, the fraction of photons incident on a particle which reappear as scattered photons. Additional subscripts are sometimes used to identify upper and lower cloud layers and to differentiate Spot layers from Zone layers. The use of superscript * or ' distinguishes continuum or scaled values, respectively.

REFERENCES

Axel, L. (1972). Inhomogeneous Models of the Atmosphere of Jupiter. Astrophys. J. *173*, 451.

Bergstralh, J. T. (unpublished). Methane Absorption in the Jovian Atmosphere II. Absorption Line Formation. (Submitted to Icarus.)

Chandrasekhar, S. (1960). Radiative Transfer. New York, Dover.

Coffeen, D. L., and Hansen, J. E. (1973). Polarization Studies of Planetary Atmospheres. In Planets, Stars and Nebulae Studied with Photopolarimetry (ed. T. Gehrels). Tucson, University of Arizona Press.

Coyne, G. V., and Gehrels, T. (1967). Wavelength Dependence of Polarization. X. Interstellar Polarization. Astron. J. *72*, 887.

Danielson, R. E., and Tomasko, M. G. (1969). A Two-Layer Model of the Jovian Clouds. J. Atmos. Sci. *26*, 889.

Deirmendjian, D. (1969). Electromagnetic Scattering on Spherical Polydispersions. New York, Elsevier.

Dick, K. A. (1974). (Kitt Peak National Observatory). Private communication to the author.

Gehrels, T., Herman, B. M., and Owen, T. C. (1969). Wavelength Dependence of Polarization. XIV. Atmosphere of Jupiter. Astron. J. *74*, 190.

Gehrels, T., and Teska, T. M. (1960). A Wollaston Photometer. Publ. Astron. Soc. Pacific *72*, 115.

Hansen, J. E. (1969a). Radiative Transfer by Doubling Very Thin Layers. Astrophys. J. *155*, 565.

Hansen, J. E. (1969b). Exact and Approximate Solutions for Multiple Scattering by Cloudy and Hazy Planetary Atmospheres. J. Atmos. Sci. *26*, 478.

Hansen, J. E. (1971). Multiple Scattering of Polarized Light in Planetary Atmospheres. Part II. Sunlight Reflected by Terrestrial Water Clouds. J. Atmos. Sci. *28*, 1400.

Hansen, J. E., and Pollack, J. B. (1970). Near-Infrared Light Scattering by Terrestrial Clouds. J. Atmos. Sci. *27*, 265.

Hess, S. L. (1951). Reports on the Project for the Study of Planetary Atmospheres. Lowell Observatory, Flagstaff, Arizona.

Hess, S. L. (1953). Variations in Atmospheric Absorption over the Disks of Jupiter and Saturn. Astrophys. J. 118, 151.

Hunt, G. E. (1973). Formation of Spectral Lines in Planetary Atmospheres. IV. Theoretical Evidence for Structure of the Jovian Clouds from Spectroscopic Observations of Methane and Hydrogen Quadrupole Lines. Icarus 18, 637.

Hunten, D. M. (1971). Composition and Structure of Planetary Atmospheres. Space Sci. Rev. 12, 539.

Kuiper, G. P. (1972). Lunar and Planetary Laboratory Studies of Jupiter, I and II. Sky and Telescope 43, 4 and 75.

Labs, D., and Neckel, H. (1968). The Radiation of the Solar Photosphere from 2000 Å to 100 μ. Zeitschrift für Astrophysik 69, 1.

Lacis, A. A., and Hansen, J. E. (1974). A Parameterization for the Absorption of Solar Radiation in the Earth's Atmosphere. J. Atmos. Sci. 31, 118.

Lewis, J. S. (1969). The Clouds of Jupiter and the NH_3-H_2O and NH_3-H_2S Systems. Icarus 10, 365.

McElroy, M. B. (1969). Atmospheric Composition of the Jovian Planets. J. Atmos. Sci. 26, 798.

Mitchell, R. I., and Johnson, H. L. (1969). Thirteen-Color Narrow-Band Photometry of One Thousand Bright Stars. Comm. Lunar and Planetary Laboratory 8, 1.

Owen, T. (1969). The Spectra of Jupiter and Saturn in the Photographic Infrared. Icarus 10, 355.

Owen, T., and Mason, H. P. (1969). New Studies of Jupiter's Atmosphere. J. Atmos. Sci. 26, 870.

Potter, J. F. (1970). The Delta Function Approximation in Radiative Transfer Theory. J. Atmos. Sci. 27, 945.

Savage, B. D., and Danielson, R. E. (1968). Models of the Atmosphere of Jupiter. In Infrared Astronomy. New York, Gordon and Breach.

Taylor, D. J. (1965). Spectrophotometry of Jupiter's 3400-10,000 Å Spectrum and a Bolometric Albedo for Jupiter. Icarus 4, 362.

Teifel, V. G. (1969). Molecular Absorption and the Possible Structure of the Cloud Layers of Jupiter and Saturn. J. Atmos. Sci. 26, 854.

van de Hulst, H. C., and Grossman, K. (1968). Multiple Light Scattering in Planetary Atmospheres. In The Atmospheres of Venus and Mars. New York, Gordon and Breach.